Materials Today Bio 29 (2024) 101327

Contents lists available at ScienceDirect

Materials Today Bio

journal homepage: www.journals.elsevier.com/materials-today-bio

"On-demand" nanosystem-integrated microneedles for amplified triple therapy against recalcitrant bacteria and biofilm growth

Ting Wen [a], Yiting Zhao [a], Yanping Fu [b], Ying Chen [b], Xiaodie Li [b], Chaonan Shi [b], Dongyi Xian [b], Wanchen Zhao [b], Dan Yang [b], Chao Lu [b], Chuanbin Wu [b], Xin Pan [a,*], Guilan Quan [b,**]

[a] School of Pharmaceutical Sciences, Sun Yat-sen University, Guangzhou, 510006, China
[b] College of Pharmacy, Jinan University, Guangzhou, 511443, China

ARTICLE INFO

Keywords:
Phototherapy
Membranolytic effect
"On-demand" release
Microneedles
Bacterial skin infection

ABSTRACT

Phototherapy has emerged to eradicate recalcitrant bacteria without causing drug resistance, but it is often accompanied by considerable limitations owing to a high tolerance of recalcitrant bacteria to heat and oxidative damage, leading to low efficiency of monotherapy and unwanted side effects. Assuming that employing antimicrobial peptides (AMPs) to disrupt bacterial membranes could reduce bacterial tolerance, a multifunctional "on-demand" nanosystem based on zeolitic imidazolate framework-8 (ZIF-8) with metal ions for intrinsic antibacterial activity was constructed to potently kill methicillin-resistant *Staphylococcus aureus* (MRSA). Then, microneedles (MNs) were used to transdermally deliver the ZIF-8-based nanosystem for localized skin infection. After MNs insertion, the nanoplatform could specifically deliver the loaded therapeutic components to bacterial infection sites through employing hyaluronic acid (HA) as a capping agent, thus realizing the "on-demand" payload release triggered by excess hyaluronidase secreted by MRSA. The prepared nanosystem and MNs were confirmed to exert an amplified triple therapy originating from membranolytic effect, phototherapy, and ion therapy, thus displaying a powerful bactericidal and MRSA biofilm destruction ability. This intelligent antimicrobial strategy may bring a dawn of hope for eradicating multidrug-resistant bacteria and biofilms.

1. Introduction

Bacteria are ubiquitous in nature, existing in, on, and around us. Due to their rapid metabolism, they can replicate within minutes. Pathogenic bacteria often attach to human skin and mucosal surfaces using specialized components, leading to skin infections. In severe cases, these infections can extend into subcutaneous tissues, causing conditions like cellulitis or carbuncles. Unfortunately, the widespread misuse of antibiotics, coupled with inappropriate infection control measures, has led to the emergence of antibiotic-resistant pathogens, including the notorious superbug methicillin-resistant *Staphylococcus aureus* (MRSA) [1]. To make matters worse, MRSA can encase bacterial communities in a self-produced extracellular polymeric matrix, forming biofilms that shield the bacteria from therapeutic agents [2]. The rise of antibiotic-resistant bacterial infections has thus intensified the research for potent new antimicrobial treatments [3,4].

Phototherapy has emerged as a promising antibacterial strategy, primarily through photothermal therapy (PTT) and photodynamic therapy (PDT). These approaches rely on photosensitizers, which are activated by specific wavelengths of light to either generate heat or convert surrounding oxygen molecules into cytotoxic reactive oxygen species (ROS) [5]. PTT is particularly advantageous due to its rapid action and efficacy without fostering drug resistance. However, bacteria have a high tolerance to temperature, creating a dilemma for PTT: moderate temperatures (around 50 °C) are insufficient to eradicate bacteria, while higher temperatures (above 60 °C) risk damaging surrounding healthy tissues. PDT, on the other hand, struggles to penetrate deeper bacterial biofilms due to the short lifespan (less than 4 μs), confined diffusion, and small coverage area of cytotoxic ROS [6,7]. As a result, recalcitrant microorganisms are difficult to eliminate using PTT or PDT alone. In addition, free photosensitizers are often prone to degradation and suffer from aggregation-caused quenching in aqueous solutions, reducing their fluorescence efficiency and overall phototherapy effectiveness [8–10].

* Corresponding author.
** Corresponding author.
E-mail addresses: panxin2@mail.sysu.edu.cn (X. Pan), quanguilan@jnu.edu.cn (G. Quan).

https://doi.org/10.1016/j.mtbio.2024.101327
Received 2 August 2024; Received in revised form 13 October 2024; Accepted 5 November 2024
Available online 6 November 2024

Porous nanoparticles (NPs) have shown promise in addressing these challenges. With their high porosity and well-defined structures, NPs can deliver photosensitizer molecules while preventing quenching and enhancing physiological stability via a steric-hindrance effect [11–13]. However, traditional NPs merely serve as carriers without any therapeutic enhancement, and uncontrolled release of photosensitizers may cause toxic side effects to normal tissues. Therefore, the development of novel, "on-demand" nanosystems that improve the delivery of photo-excited antimicrobial agents is urgently required. Among the various alternatives, metal-organic frameworks (MOFs) have gained attention for their unique properties, including tunable composition and structure, high surface area, easy of functionalization, and excellent biodegradability [14–16]. One of the most studied MOFs, Zeolitic imidazolate framework-8 (ZIF-8), is composed of tetrahedral zinc centers bridged by 2-methyl imidazole (2-MeIM) ligands through coordination bonds [17,18]. ZIF-8's acid-responsive disassembly property, triggered by protonated ligands at acidic pH [19], makes it particularly attractive for antibacterial applications, as the microenvironment of bacterial infections and biofilms is inherently acidic (pH 4.5–6.5) [20]. Once disassembled, ZIF-8 releases zinc ions (Zn^{2+}) which disrupt bacterial ion channels, disturb the environmental ionic balance, and produce free radicals [21–23].

In addition to MOFs, various materials, including antimicrobial peptides (AMPs), 2D nanosheets (MXenes [24–26], molybdenum disulfide [27], single-layered graphene [14]), bacteriophages [28,29], and lysins [30,31], have been explored for their ability to perforate bacterial membranes and interact with intracellular components. Among these, AMPs are naturally occurring alkaline peptides with strong cationic properties, many of which have an isoelectric point greater than 7 [32]. As an AMP naturally produced by *Streptomyces albulus*, ε-poly-L-lysine (PL) contains 25–30 lysine residues, which has strong bactericidal activity and thermal stability (120 °C, 20 min) [33]. PL's mechanism involves electrostatic attraction to bacterial membranes, leading to membrane disruption and ion leakage, ultimately causing bacterial death. Due to its unique mode of action, PL has a low propensity for developing drug resistance, making it a viable alternative to traditional antibiotics.

Building on these findings, we hypothesize that disrupting bacterial membranes first can reduce bacterial thermal tolerance and enhance the penetration of ROS, resulting in synergistic therapeutic effects. In this study, we designed a multifunctional core-shell nanocomposite with intelligent responsiveness and self-activating capability for treating bacterial infections. The core consists of the photosensitizer indocyanine green (ICG) encapsulated within a ZIF-8 skeleton (ZIF-8-ICG, ZI), while the PL is physically adsorbed onto the surface (PL@ZI, PZ). To enable "on-demand" release, we further coated the nanocomposite with a hyaluronic acid (HA) shell, creating a hybrid nanosystem (PL@ZI-HA, PZH). Many bacteria, including *S. aureus* and MRSA, secrete virulence-related enzymes like hyaluronidase (HAase) [34–36], which degrades HA to trigger responsive payload release in the bacterial microenvironment.

The PZH NPs were delivered using a transdermal microneedle (MN) patch (PZH MNs) for targeted treatment of MRSA-induced skin infections (Scheme 1A). Upon application, the PZH MNs patch non-invasively penetrated the stratum corneum, physically disrupting microbial biofilm architecture [37–39]. In the presence of HAase, the HA layer was cleaved, exposing PL with its reactive positive charge [40,41], leading to membrane disruption, massive leakage of intracellular contents, and potentiated phototherapy. NIR light activation of ICG induced both localized heat and ROS production, causing damage to bacterial proteins, nucleic acids, and lipids. Simultaneously, ZIF-8 released Zn^{2+} ions (Scheme 1B), further enhancing the antibacterial effect by disrupting bacterial ionic balance and producing free radicals.

Our results demonstrate that this PZH nanosystem and PZH MNs patch exhibit significant antimicrobial activity against recalcitrant MRSA, offering a promising alternative for treating multidrug-resistant bacterial skin infections through a triple therapy originated from membranolytic effect, phototherapy, and ion therapy.

2. Materials and methods

2.1. Materials

Zinc nitrate hexahydrate [$Zn(NO_3)_2{\cdot}6H_2O$], 2-MeIM, ICG, polyvinyl alcohol (PVA), and polyvinylpyrrolidone (PVP) K30 were purchased from Aladdin Biochemical Technology Co., Ltd. (Shanghai, China). Methanol was provided by Tianjin Zhiyuan Chemical Reagent Co., Ltd. (Tianjin, China). PL was acquired from Bainafo Bioengineering Co., Ltd (Zhengzhou, China). HA was supplied by Bloomage Freda Biopharm Co., Ltd. (Shandong, China), and HAase was purchased from Solarbio Technology Co., Ltd. (Beijing, China). PVP K90 was kindly donated by BASF SE (Ludwigshafen, Germany). 1,3-Diphenylisobenzofuran (DPBF) was provided by Sigma-Aldrich Trading Co., Ltd. (Shanghai, China), and 2,7-dichloride hydrofluoresceinpreci diacetate (DCFH-DA) was obtained

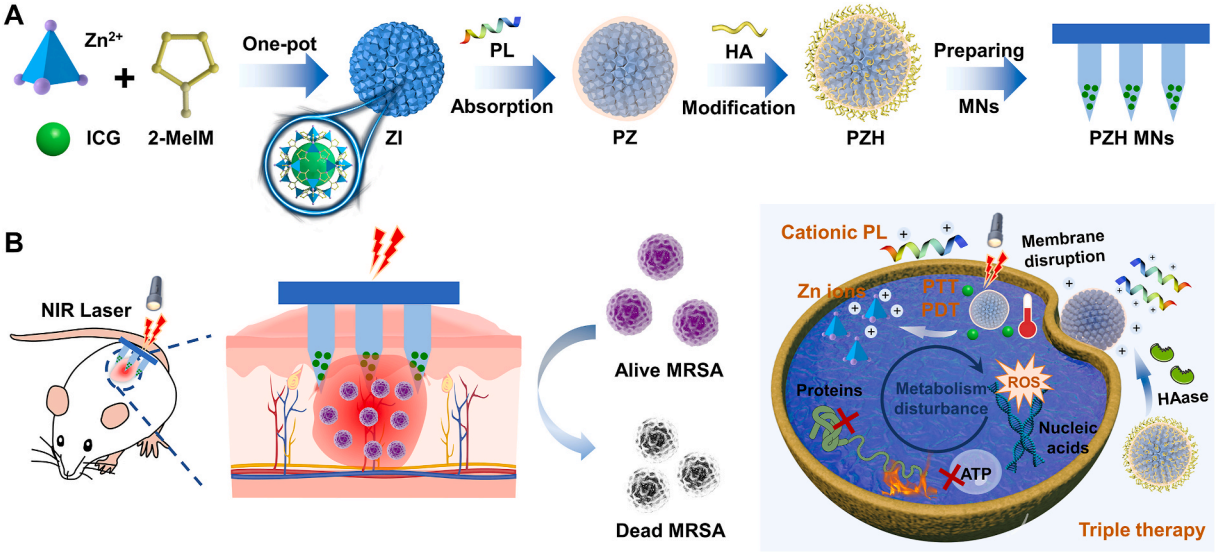

Scheme 1. (A) The preparation of "on-demand" nanosystem-integrated microneedles (PZH MNs). (B) Schematic illustration of the amplified triple therapy (membranolytic effect, phototherapy, and ion therapy) against recalcitrant bacteria-induced skin infections.

from Solarbio Technology Co., Ltd, Beijing, China). Mueller-Hinton agar (MHA) and Mueller-Hinton broth (MHB) were supplied by Oxoid (Basingstoke, England). All the reagents were used as received without further purification.

2.2. Synthesis and characterization of nanosystem

2.2.1. Preparation of nanoparticles

Firstly, ZI nanoparticles were facilely synthesized via the modified one-pot synthesis method according to our previous work [19]. ICG (30 mg) was dissolved in 3 mL of methanol containing 90 mg of $Zn(NO_3)_2 \cdot 6H_2O$ (solution A), and 198 mg of 2-MeIM was dissolved in an equal volume of methanol (solution B). Then solution B was dropped into solution A under continuous stirring at 300 rpm for 1 h. The final ZI NPs were obtained after centrifugation and redispersed with ultrapure water.

Then, PL aqueous solution was dropwise added to ZI suspension (v/v 1:1) and stirred at 500 rpm for 1 h, which was collected by centrifugation to generate PL@ZI. For further surface coating, PZ dispersion (4 mg/mL) was mixed with HA solution (0.2 mg/mL) of the same volume to prepare PZH. Fluorescence spectroscopy (FluoroMax-4, HORIBA Instruments Incorporated) was applied to quantify the ICG loading capacity, and high-performance liquid chromatography (HPLC, LC-20AT, Shimadzu, Japan) was used to determine the free PL content in the supernatant to calculate the adsorbing capacity.

2.2.2. In vitro photothermal conversion and ROS generation detection

The photothermal conversion ability of ICG, ZI, PZ, and PZH activated by NIR irradiation was respectively determined. The sample solution (1 mL) containing 5, 10, or 20 μg/mL of ICG was irradiated by a NIR laser (808 nm, 1.0 W/cm^2) for 10 min. The effect of different power densities was also investigated. An infrared thermal imager (TiS75, Fluke, Shanghai, China) was applied to monitor and record the solution temperature.

The photodynamic effect of ZI, PZ, and PZH was carried out using DPBF as a ROS indicator. In brief, the mixture solution containing 10 μg/mL of ICG and 75 μM of DPBF was irradiated for 10 min (808 nm, 1.0 W/cm^2), and the UV–visible spectra were recorded at predetermined time points.

2.2.3. Microenvironment-responsive property and storage stability

To confirm the outer HA layer modification, PZH was incubated with HAase (150 U/mL) overnight to observe the change of zeta potential. Besides, the lattice structure of PZH was performed by powder X-ray diffractometer (pXRD). After immersion in pH 5.4 PBS for 24 h, the morphology of NPs was observed by transmission electron microscope (TEM) to investigate the pH-responsiveness of the ZIF-8 skeleton. To evaluate the storage stability, the ICG content of PZ or PZH aqueous suspension was measured by Fluorescence spectroscopy at predetermined time intervals.

2.3. In vitro antibacterial activity

In this study, MRSA was selected as the representative gram-positive bacteria strain. MRSA was firstly inoculated into MHB medium on a 37 °C shaker overnight and then adjusted to the concentration of 2 × 10^5 CFU/mL. The diluted MRSA suspension (500 μL) was cultured with an equal volume of PBS, PL, ZI, or PZH for 2 h, and performed with NIR laser irradiation for 10 min. The solution temperature change was detected by the infrared thermal imager. Finally, the bacterial suspensions were 10-fold diluted serially, and 10 μL was spread onto MHA plates, followed by incubation for 24 h to count the colony forming unit (CFU).

2.4. Relevant antimicrobial mechanisms

2.4.1. Bacterial membrane integrity and morphological changes

The destruction of bacterial membrane integrity after various treatments was qualitatively assessed using a Live/Dead bacteria staining kit (SYTO 9/PI, Thermo Fisher Scientific, Waltham, USA). Briefly, MRSA suspension (1 × 10^8 CFU/mL, 500 μL) was separately treated with 500 μL of different samples for 2 h and followed by exposure to laser irradiation for 10 min. After another 2 h of incubation, bacteria were collected by centrifugation at 8000 rpm for 5 min and washed with sterile PBS twice. The precipitate was resuspended in 500 μL of premixed dye solution (SYTO 9 30 μM, PI 5 μM) at room temperature and stained in the dark for 30 min. After removal of excess dye by washing 3 times, bacterial samples were dispersed with PBS and then imaged using a confocal laser scanning microscope (CLSM, FV3000, Olympus Corporation, Japan).

Then, a biological scanning electron microscope (SEM, SU8010, Hitachi, Japan) was used to inspect the morphological changes of MRSA. The pretreated bacterial cells were centrifuged at 4000 rpm for 10 min, rinsed twice with PBS, and immediately fixed with 2.5 % glutaraldehyde overnight at 4 °C. Then the bacteria were treated with gradient ethanol solution and dehydrated for 15 min in each step, followed by observation using SEM.

2.4.2. Adenosine triphosphate (ATP) activity assay

Bacterial metabolic activity was assessed by measuring the bacterial ATP level using the Enhanced ATP Assay Kit (Beyotime Biotechnology, Shanghai, China). Briefly, MRSA was pretreated with different samples followed by laser exposure and precipitated by centrifugation at 4 °C. Then, 200 μL of lysate was added to lysate the bacterial cells in an ice bath. After lysis, samples were centrifuged at 12000 rpm for 5 min under 4 °C to collect supernatant, which was subsequently added to a sterile 96-well white plate supplemented with 100 μL of ATP test solution. The ATP luminescence signals were recorded by a multifunctional microplate reader (Flex Station 3, Molecular Devices, USA).

2.4.3. Intracellular content leakage detection

To investigate the cellular content leakage caused by the disruption of the cell membrane, MRSA bacteria (1 × 10^8 CFU/mL) were pretreated with different samples, irradiated with NIR laser for 10 min, and immediately centrifuged at 12000 rpm for 5 min under 4 °C. The supernatant was collected and stored in an ice bath. The concentration of leaked proteins of each group was quantified using a BCA Protein Assay kit. Besides, the optical density (OD) values at 260 nm and 280 nm were recorded on behalf of extracellular nucleic acids and proteins released by bacterial cells, respectively.

2.4.4. Intracellular ROS detection in bacteria

The level of ROS generated in bacteria was qualitatively detected. Different samples were inoculated with MRSA bacterial suspension (1 × 10^8 CFU/mL, 500 μL) for 2 h. The resulting mixture was irradiated by NIR laser, centrifuged, and washed three times with PBS. Precipitates were collected, resuspended in 1 mL of DCFH-DA probe (a final concentration of 10 μM) for 30 min, and finally imaged using CLSM.

2.5. Biofilm disruption and penetration behavior

To obtain biofilm culture, an aliquot of adjusted MRSA suspension (2 × 10^7 CFU/mL, 500 μL) was added to a laser confocal 24-well plate. After cultivation in a 37 °C incubator for 72 h, mature MRSA biofilm was obtained. Different drug dispersions (500 μL) were added, followed by 808 nm NIR irradiation for 10 min, and rinsed carefully with sterile PBS twice. SYTO 9 dye solution (30 μM) was added to stain bacteria in the dark for 30 min. After the removal of the excess dye, fluorescent images were taken by CLSM. For the quantitative analysis of residue living bacteria within the biofilm, MRSA suspension was inoculated in a 96-

well plate following the same steps above. Viable bacteria were quantified by the agar plate colony-counting method. The biofilm-penetration behavior of nanosystems was implemented to figure out material-bacteria interaction [42]. The biofilm was incubated with ICG, ZI, PZ, or PZH for 4 h, stained with 150 μL of diaminophenyl indole (DAPI), followed by imaging using CLSM.

2.6. Fabrication and characterization of NPs-loaded microneedles

The NPs-embedded microneedles were fabricated through a modified three-step centrifugation method [9,43]. In brief, the nanoparticle aqueous suspension was mixed with PVA/PVP K30 to form the needle matrix solution (v/v 4:1), which was injected into the negative mold and centrifugated at 4000 rpm for 5 min under 4 °C. After removing the excess solution, the negative mold was centrifuged for 30 min and dried overnight in a desiccator. Then, PVA/PVP K30 mixture solution (50/300 mg/mL) was filled into the mold under the same centrifugation conditions. Finally, PVP K90 ethanol solution (w/v 1:3.2) was employed to form the base part via centrifugation. After drying for 48 h, the NPs-loaded MNs were gently peeled off.

The morphology of fabricated MNs was observed with SEM (EVO MA10, Carl Zeiss AG, Germany), a digital camera, and an inverted microscope (Eclipse Ts2, Nikon Corporation, Tokyo, Japan). The fracture force of the MNs was examined by a texture analyzer (CT3, Brookfield, USA) [44,45]. To further assess the skin insertion capability, a piece of MN patch was inserted into the mouse back skin *(in vivo)* or shaved rat dorsal skin (*ex vivo*) for 2 min. After peeling off the patch, the residue MNs and insertion site were imaged with a digital camera. SEM was applied to observe the dissolution of the microneedle patch, and hematoxylin and eosin (H&E) staining was performed to observe the histological character of the punctured skin. The photothermal performance of PZH NPs@ MNs was monitored for 20 min. The particle size was measured to confirm the recovery of intact nanostructures following microneedle administration.

2.7. In vivo antimicrobial efficiency assessment

Four-week-old ICR (CD-1) mice ordered from Guangdong Medical Laboratory Animal Center were used for the *in vivo* antimicrobial experiments. The animal experimental procedures were performed with the approval of the Animal Ethics Committee of Sun Yat-sen University (SYSU-IACUC-2022-B0874). Briefly, PBS containing 2×10^8 CFU/mL of MRSA (50 μL) was subcutaneously injected into the shaved back of each mouse to establish the bacterial infection model. After 24 h of inoculation, the mice equipped with abscess were randomly divided into 7 groups: no treatment, commercial mupirocin ointment (Bactroban, SK&F, Tianjin, China), PL MNs, ZI MNs + NIR, PZ MNs + NIR, PZH MNs, and PZH MNs + NIR. Two hours after the patch treatment, NIR irradiation was performed for 20 min, throughout which the temperature was monitored. Then the mice were euthanized and the infected back skin was excised to homogenize with 1 mL of sterile PBS, diluted by a 10-fold series, and spread onto the MHA plates for MRSA quantification. The abscess sites of mice were photographed.

2.8. In vivo inflammatory response and histological analysis

The degree of inflammatory response was quantitatively evaluated according to the expression level of the representative inflammatory cytokines in the skin homogenates, including interleukin 6 (IL-6) and tumor necrosis factor-α (TNF-α). In brief, the homogenates were centrifuged at 8000 rpm for 20 min under 4 °C to obtain corresponding supernatants for cytokine concentration determination via the enzyme-linked immunosorbent assay (ELISA) kit based on the manufacturer's instructions. Beyond that, the back skin lesions after treatment were excised and fixed in 4 % paraformaldehyde for H&E and Gram staining.

2.9. In vivo safety evaluation

Healthy ICR mice were randomly divided into 3 groups: No treatment (normal), PZH MNs, and PZH solution (abbreviated as PZH aq), in which 100 μL of PZH aq (2 mg/mL) was subcutaneously injected into the back skin of mice. In order to observe the short-term and long-term toxicity of the preparations, mice were euthanized 5 h and 5 d after administration, respectively. The local skin and main organs were taken for histological analysis, and whole blood samples were collected for blood routine determination. To investigate skin recovery after the MNs application, healthy ICR mice were divided into 4 groups: Normal, PL MNs, ZI MNs, and PZH MNs. The skin recovery of mice was pictured at predetermined time points post-administration.

2.10. Statistical analysis

All data were presented as mean ± standard deviation (SD). Statistical analyses were performed using a *t*-test or one-way analysis of variance (*ANOVA*) via Graphpad Prism 9 (Graphpad Software LLC., San Diego, USA). P value < 0.05 was considered statistically significant.

3. Results and discussion

3.1. Preparation and characterization of PZH

ZIF-8 is one of the most widely applied MOFs for drug delivery, which enjoys a high reputation for its large specific surface area, high porosity, and structural sensitivity to acid environments. Herein, it is chosen for stabilizing active therapeutics, that is ICG and PL, also because the zinc ions that constitute the ZIF-8 backbone can exert an auxiliary antibacterial outcome [46]. ZI nanoparticles were firstly synthesized through one-pot drug encapsulation, which would be less likely to influence the ICG activity. Due to the negative charge of sulfonic groups in ICG molecules, the obtained NPs were equipped with an average zeta potential of −9.63 mV (Table S1, Fig. 1A). Then, PZ with the reversed surface charge of +15.60 mV was formed for that PL rich in cations had a strong electrostatic force with ZI. The surface absorption of the HA shell layer rendered PZH electronegative again (−9.47 mV). The average hydrodynamic size of PZH (162.9 nm) measured by dynamic light scattering (DLS) was slightly increased relative to 137.8 nm for ZI and 147.5 nm for PZ (Fig. S1), which were larger than their particle diameters as indicated by the TEM images (Fig. S2).

Fig. S3–S4 presented the UV–Vis absorption and fluorescence emission spectra of the samples, with the characteristic peaks appearing after ICG encapsulation, while PL and HA exhibited broad UV absorption at 200–300 nm and no fluorescence. The ICG payload was calculated to be ~10.67 % as determined by the calibration curve shown in Fig. S5, and the PL absorption capacity was determined to be 98.34 %. As shown in Fig. S6, the crystalline diffraction peaks of ZIF-8 were retained for each sample, indicating that the whole preparation process would not destroy the skeleton structure. The Fourier transform infrared spectroscopy (FT-IR) was also conducted to further substantiate the ICG encapsulation, PL absorption, and HA coating. Fig. S7 demonstrated that the characteristic peak of ICG bending vibration around 1080 cm^{-1} could be observed in the spectra of ZI, PZ, and PZH. The FT-IR spectrum of PL exhibited the stretching vibration at 1400 cm^{-1} ascribed to the C–N single bond in amide, which appeared in the spectra of PZ and PZH as expected, suggesting the successful deposit of PL on the ZI surface. Compared with PZ, the fundamental band at 1620~1720 cm^{-1} corresponding to the stretching vibration of the carbonyl group (–C=O) and the broad band around 3200~3600 cm^{-1} attributed to the stretching vibration of the hydroxyl group (–OH) in PZH verified the successful modification of HA layer. The X-ray photoelectron spectroscopy analysis displayed a positive result with Zn element referring to ZIF-8 and S along with Na elements referring to ICG, which could further demonstrate the successful preparation of the drug-loaded hybrid NPs (Fig. S8).

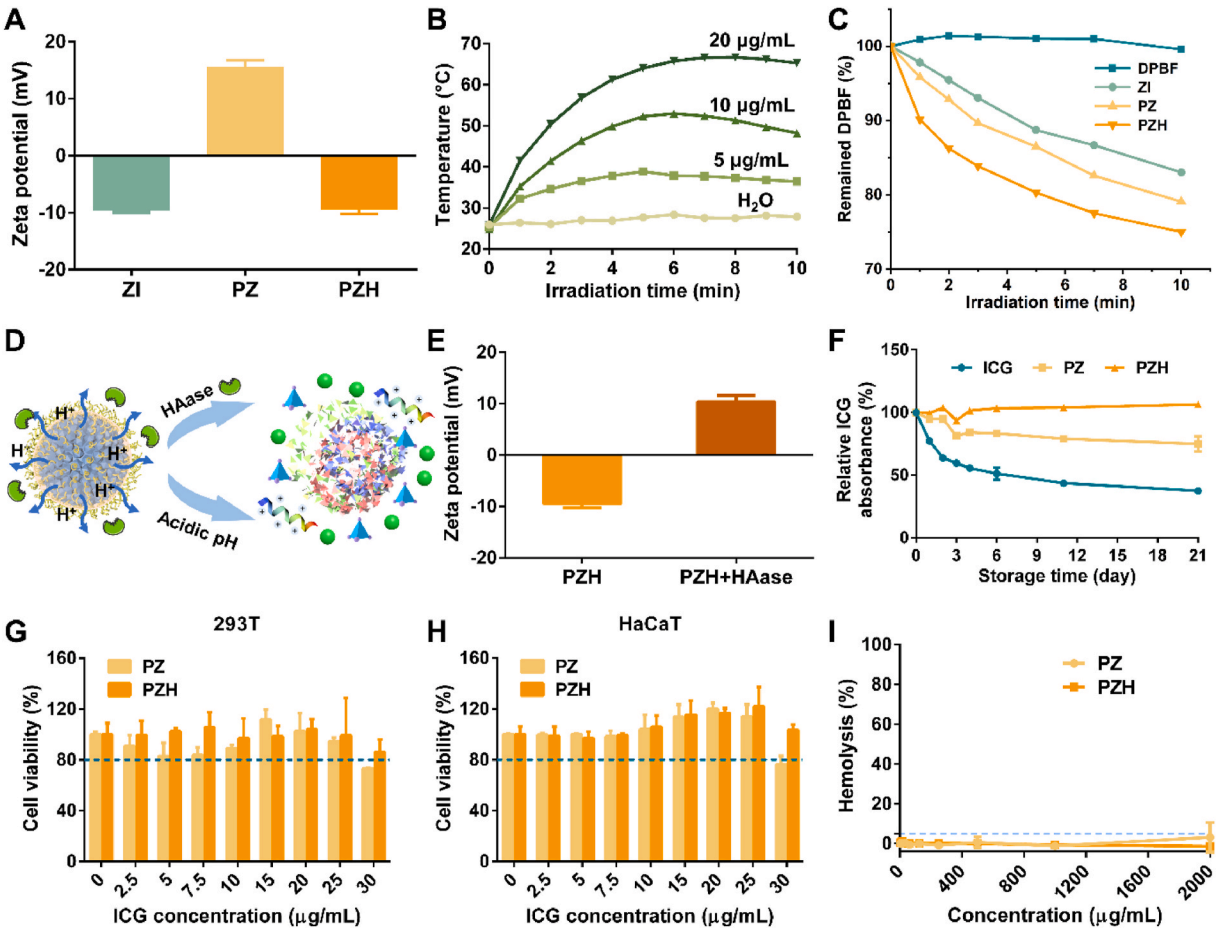

Fig. 1. Characterization of ZI, PZ, and PZH. (A) The zeta potential of the prepared NPs ($n = 3$). (B) The NIR photothermal conversion performance of PZH solution at various concentrations (1.0 W/cm^2). (C) The decrement curve of DPBF absorbance at 416 nm under laser irradiation (808 nm, 1.0 W/cm^2). (D) Schematic illustration of microenvironment-responsive degradation of PZH nanosystem. (E) The change of PZH zeta potential after incubation with HAase ($n = 3$). (F) The storage stability of ICG, PZ, and PZH aqueous solution relative to day 0 (denoted as 100 %) ($n = 3$). (G) 293T and (H) HaCaT cell viabilities after incubating with various concentrations of PZ or PZH ($n = 3$). (I) Hemolytic activities of PZ and PZH ($n = 3$). The blue dashed line indicates 5 % hemolysis. (For interpretation of the references to colour in this figure legend, the reader is referred to the Web version of this article.)

3.2. *In vitro photothermal conversion and ROS generation detection*

As the only FDA-approved substance for *in vivo* imaging, ICG, a biocompatible photosensitizer, can convert optical energy into heat and meanwhile generate ROS. As shown in Fig. S9, the temperature of free ICG solution (20 μg/mL) raised to 52 °C when irradiated by 808 nm laser (1.0 W/cm^2). By contrast, the temperature of ZI and PZH solution evidently rose to 73 °C and 67 °C respectively (Fig. 1B, S10-S11), from which it could be referred that the ICG encapsulation into the ZIF-8 network helped avoid its aggregation-caused quenching on account of spatial confinement. Comparing ZI and PZH at the same concentration, it was found that the surface HA coating might have a weak masking effect on the heating effect, but the overall effect was not significant. In addition, with the increase of ICG concentration, the photothermal conversion performance of the solution was also strengthened, indicating the feasibility of tunable photothermal efficiency. A similar result was also presented as output power-dependent temperature elevation for the PZH nanosystem (Fig. S12).

Next, the *in vitro* photoinduced ROS generation ability was evaluated by DPBF. In Fig. 1C and S13, When DPBF was incubated with ZI, PZ, and PZH (ICG: 10 μg/mL), the absorbance at 416 nm continuously declined over time under the exposure of irradiation, as compared to the negligible change of pure DPBF probe. The results well demonstrated that the restriction of ZIF-8 skeleton on the ICG aggregation and the greatly strengthened photostability was conducive to exerting a superior PDT effect.

3.3. *Microenvironment-responsive characteristic and storage stability*

As reported, the bacterial infection microenvironment is typified by overexpressed specific enzymes and low pH owing to sugar fermentation [36]. To confirm the microenvironment-responsive property (Fig. 1D), PZH was incubated with HAase to specifically enzymolyse the HA adhesion layer. Fig. 1E showed that in the presence of HAase, the average zeta potential of PZH reversed from a negative to a positive charge. As presented in Fig. S14A, the incubation with HAase would not affect the PZH lattice structure, whereas the pH change appeared to cause the partial collapse of the ZIF-8 skeleton, for that the crystalline characteristic peak at 2θ of 7.3° vanished and other peaks also weakened to some extent. The TEM image in Fig. S14B displayed that PZH NPs under low pH conditions almost lost their original morphology, with a tangled structure and irregular shape observed. These results demonstrated that our prepared PZH nanosystem possessed the microenvironment-responsive property, conducive to exerting a targeted therapeutic effect.

The stability of ICG loaded in PZ and PZH was determined over 21 d storage at 4 °C. As displayed in Fig. 1F, the free ICG rapidly degraded to 59.7 % (day 3) and 37.4 % (day 21). For PZ, the ICG content remained at 81.3 % and 74.9 % after 3 and 21 days of storage. Attractively, the loaded ICG content in PZH consistently maintained above 93 % for 21

days, which indicated superior ICG stability owing to the entrapment of porous ZIF-8 framework and subsequent HA coating.

3.4. *In vitro* biocompatibility

3.4.1. *Cytotoxicity study*

Primarily, high selectivity and good biocompatibility of materials are essential prerequisites for their biomedical applications. Thereby, the *in vitro* cytotoxicity on kidney 293T cells and human immortalized epidermal cells (HaCaT) of nanosystems was carried out. As shown in Fig. 1G and H, as the concentration increased, PZ started to show cytotoxicity against both types of cells, and the final cell survival rate was below 80 %. Regarding PZH with HA coating, the survival rates of both 293T and HaCaT cells were all above 80 %, implying that the outer HA shell modification endowed PZH with good cytocompatibility.

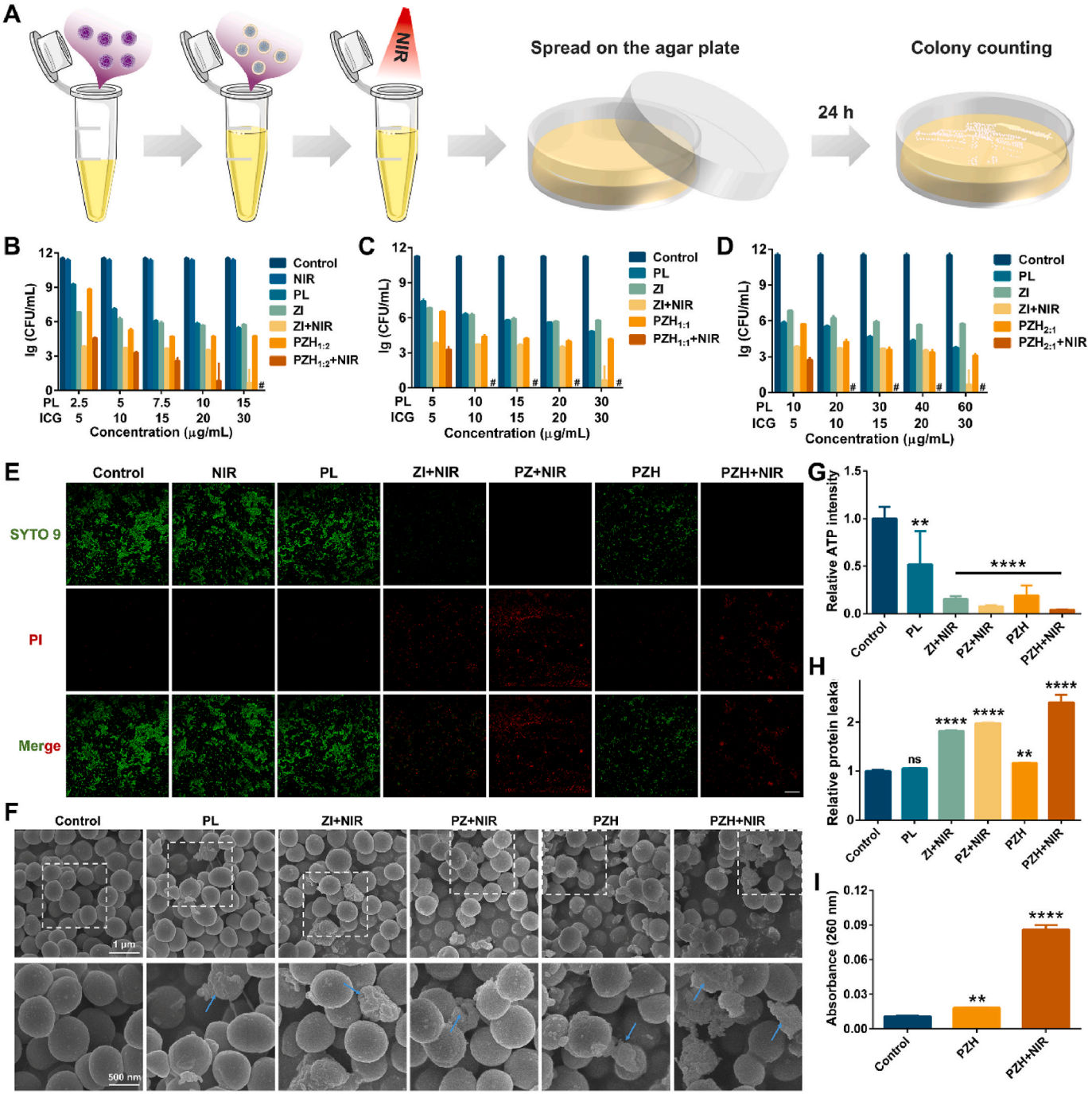

Fig. 2. *In vitro* antibacterial activities against MRSA and the antimicrobial mechanisms. (A) Schematic illustration of antibacterial test by agar plate counting method. (B–D) Quantitative bacterial viability by lg (CFU/mL) after various treatments with or without NIR laser irradiation for 10 min (808 nm, 1.0 W/cm^2). Data are presented as mean ± SD ($n = 3$), and # represented that no colonies were observed. (E) CLSM images of Live/Dead bacteria staining assay (scale bar: 30 μm). The concentrations of PL and ICG were all 20 μg/mL. (F) Biological SEM images of MRSA after different treatments. The arrows signified the morphological damage (scale bar: 500 nm). (G) Quantified bacterial ATP activity relative to the control ($n = 3$). (H) Relative intracellular protein leakage from treated MRSA ($n = 3$). (I) The absorbance at 260 nm of released nucleic acids from MRSA ($n = 3$). Note: ns signified no significant difference *vs* control, $^{**}p < 0.01$ *vs* control, $^{****}p < 0.0001$ *vs* control. The concentrations of PL and ICG in (F-I) were all 30 μg/mL.

3.4.2. Hemolysis assay

PZ and PZH were then incubated with fresh mammalian erythrocytes to assess their hemolytic activities (Fig. 1I). Attractively, PZH induced negligible hemolysis even at concentrations up to 2 mg/mL, always remaining below 2 %, which suggested its outstanding selectivity for anionic microbial membranes but not zwitterionic mammalian cell membranes. By contrast, PZ showed a slightly higher hemolytic activity of 3.2 % ± 7.6 % at 2 mg/mL. The underlying mechanism that helped interpret the difference in the hemolysis behavior of PZH was still attributed to the biocompatible HA coating. Overall, the synthetic PZH achieved an optimal balance between its antibacterial and hemolytic activities, which could be expected to serve as a powerful weapon against bacterial infections with a high curative effect.

3.5. In vitro antimicrobial effect

As mentioned before, some bacteria would secrete HAase, which could be utilized to design HA-modified nanosystem for targeting specific bacterial infections. Among them, MRSA is the most representative Gram-positive bacterium, as MRSA is resistant to many conventional antibiotics and is often associated with hospital infections. So we next evaluated the antimicrobial effect of the prepared nanosystems against MRSA (Fig. 2A).

Compared to control without treatment, NIR irradiation alone exhibited almost no germicidal effect (Fig. 2B). As a common biological preservative, PL presented a moderate antimicrobial efficacy at concentrations ranging from 2.5 to 60 μg/mL (Fig. 2B–D). Specifically, PL reduced ~3.8 and ~6.4 lg CFU/mL against MRSA at the concentration of 5 μg/mL and 30 μg/mL, respectively. The antibacterial mechanism was mainly based on its positive charge, which helped interact directly with the electronegative bacterial membranes, disrupting the cell structure of microorganisms. For ZI, the sterilization efficiency was significantly strengthened in the presence of NIR. Not surprisingly, the combinatorial treatment PZH + NIR achieved the maximum antimicrobial effect at all the same concentrations as monotherapy, benefiting from the cationic antimicrobial peptide, elevated temperature combined with toxic ROS, and concomitant zinc skeleton component.

For better comparison, the ICG concentrations were fixed while the concentrations of PL were varied proportionally to explore their synergistic effect. When the ratio of PL and ICG was set as 1:2 ($PZH_{1:2}$), 100 % MRSA killing was achieved with PZH containing 15 μg/mL of PL and 30 μg/mL of ICG, during which the temperature reached 52 °C as shown in Fig. S15A–B. However, when the ratio was increased to 1:1 ($PZH_{1:1}$) and 2:1 ($PZH_{2:1}$), PZH containing only 10 μg/mL of ICG was competent to realize a complete bactericidal effect. In these two groups, the solutions were both only heated to 40 °C (Fig. S15C–D), which would well protect other normal tissues from thermal damage. Collectively, $PZH_{1:1}$ exerted the best synergistic effect at the lowermost concentration and temperature, and the corresponding plate-counting results were presented in Fig. S16. Thereby, we speculated that $PZH_{1:1}$ could bring their superiority into full play, and was therefore selected for the subsequent in-depth studies.

3.6. Antibacterial mechanisms of PZH

3.6.1. Bacterial membrane integrity

To investigate the antimicrobial mechanisms of the nanosystem, Live/Dead bacteria staining assay was first employed to assess the bacterial membrane integrity. As presented in Fig. 2E, after treatment with PBS or NIR alone, almost all MRSA bacteria survived and emitted bright green fluorescence, which was consistent with the colony-counting results (Fig. 2B). Regarding PL and PZH without NIR irradiation, a relatively weak red fluorescence was observed. In the group of ZI + NIR, the intensity of green fluorescence was significantly diminished and the proportion of dead bacteria with red fluorescence increased. After exposure to PZ + NIR and PZH + NIR, MRSA with green fluorescence was no longer in existence instead of all stained predominately with red PI dye, suggesting that most of the bacteria cells were metabolically devitalized. These results corroborated those obtained by the *in vitro* plate-counting assay, underlining the superior synergistic effect of AMPs, phototherapy, and metal ions.

To further clarify the disorganization ability of bacterial membranes, the morphology of treated MRSA was visualized by SEM (Fig. 2F). The MRSA without any treatment maintained the typical spherical shape with smooth surfaces and intact membrane. On the contrary, damaged MRSA cells with various degrees of morphological deformity were clearly observed after incubation with different samples. Of particular note, MRSA treated by PZH + NIR exhibited the most drastic membrane destruction with clearly observed wrinkled surfaces and irregular edges, demonstrating that the triple therapy originated from PZH + NIR could strongly disrupt the bacterial cellular membrane integrity, which may subsequently trigger the leakage of cellular contents and eventually lead to cell death.

3.6.2. Bacterial ATP activity assay

To figure out the effect of our prepared nanosystems on the bacterial metabolic activity, the cellular ATP level of treated MRSA was quantitatively determined. As shown in Fig. 2G, compared with PBS control, approximately 48 % ATP was depleted in the group of PL, suggesting the positive influence of AMPs on interfering with bacterial metabolic processes. Regarding ZI + NIR and PZH, approximately 85 % and 81 % impairment of ATP activity occurred, respectively, potentially leading to a metabolic crisis. In the group of PZH + NIR, the lowest ATP level with only 4 % remaining implied a marked inhibition of metabolism and gave rise to the dramatic loss of bacterial viability.

3.6.3. Intracellular content leakage detection

As mentioned above, when the bacterial membrane integrity was impaired with perforated surfaces, the leakage of intracellular components would be triggered. First, the cytoplasmic protein leakage was assayed according to the BCA principle [47]. A more pronounced increase of leaked proteins was observed in those groups with light irradiation assistance, especially in the PZH + NIR group (~2.4-fold that of control) (Fig. 2H). In Fig. S17, the OD value at 280 nm was thus evaluated since most proteins had a characteristic maximum absorption at 280 nm. The PZH + NIR group resulted in as much as 2.7 times more protein leakage than the control. Besides, the leakage of DNA and RNA from the moribund MRSA bacteria could bring about bacterial dysfunction and apoptosis [48]. Clearly, MRSA incubated with PZH + NIR induced the largest amount of intracellular DNA and RNA leakage, up to 8 times higher than the control group (Fig. 2I).

3.6.4. Intracellular ROS generation in MRSA

The intracellular ROS generation was further detected in treated MRSA employing DCFH-DA probe, which could be oxidized by ROS to DCF with green fluorescence. As presented in Fig. S18, PBS-treated MRSA only emitted a very faint green fluorescence, while bacteria processed with ZI plus NIR produced a moderate DCF fluorescence. Not surprisingly, those bacterial cells treated by PZH and subsequent NIR irradiation displayed apparently strengthened green fluorescence, revealing the production of abundant ROS. It was worth mentioning that PZH was able to generate more ROS than ZI under light conditions, which was also consistent with the *in vitro* results shown in Fig. 1C, presumably because the PL adsorption and HA modification further helped enhance the stability of ICG, thus enabling better PDT efficacy.

To sum up, after the HA layer was enzymatically hydrolyzed in the local lesion's microenvironment, the cationic PL directly interacted with the bacterial surface and exerted the membranolytic effect, which would be also assisted by the sustained released Zn^{2+}, leading to the massive leakage of intracellular proteins and nucleic acids. The local hyperthermia and generated ROS originating from phototherapy functioned via perturbing the bacterial structure, oxidizing inner components, and

destroying the enzyme activities. The ATP synthesis process and the respiratory electron transport chain were also intercepted for compromised energy metabolism. Altogether drug-resistant MRSA could be readily inactivated in this course.

3.7. Biofilm disruption and penetration performances of PZH

Bacterial biofilm is a mass of bacterial aggregates formed by bacteria adhering to contact surfaces, secreting polysaccharide matrix, fibronectin, and lipoprotein, and encasing themselves in the pellicle [49]. Compared to the planktonic confreres, bacteria in biofilms are more drug-resistant and not susceptible to being attacked. During pellicle formation, the biofilm development was qualitatively assessed by SYTO 9 staining [50]. As depicted by Fig. 3A, the untreated biofilm exhibited a relatively compact green fluorescence. The biofilm was greatly attenuated in the groups of PZH-L + NIR (20 μg/mL of ICG) and PZH-H + NIR (30 μg/mL of ICG), indicating the disintegration of the bacterial pellicle. The superior anti-biofilm performance of PZH nanosystem was attributed to the mutually reinforced triple therapy, which altogether damaged polysaccharides, proteins, and nucleic acids that consisted of MRSA biofilm structure, subsequently inactivating the inner bacteria (Fig. 3B). Other treatments also exerted moderate destruction of biofilm. To further visualize their anti-biofilm efficacy, the residue living bacteria were quantitatively assayed (Fig. 3C–E). Consistent with the biofilm staining, the anti-biofilm activity of PZH + NIR was the most pronounced even at different concentrations, eradicating more than 99.30 % alive MRSA enclosed in biofilm.

Encouraged by the excellent anti-biofilm performances of the nanosystems, bacteria-targeting behaviors of ZI, PZ, and PZH were investigated on MRSA biofilm (Fig. 3F). Pearson's correlation coefficients between bacteria and different samples were calculated to evaluate the biofilm permeability. Coefficient ranging −1.0~0.5 means no colocalization relationship, while 0.5–1.0 means co-located. Therefore, it could be considered that there was no obvious colocalization relationship between MRSA and ICG or ZI, whereas PZ and PZH were shown to have a colocalization with bacteria. The low penetration behavior of ZI was speculated to be ascribed to its negative charge. Although the colocalization coefficients of PZ and PZH were approximate, PZH emitted a much stronger ICG fluorescence than PZ, presumedly due to the HA-mediated targeting ability of PZH to MRSA. The biofilm-penetration ability provided concrete evidence of the effective bacteria eradication and biofilm destruction ability of the PZH nanosystem under light conditions.

3.8. Fabrication and characterization of PZH MNs

Bacterial skin infections can generally be treated with topical or oral medications. However, the former is often accompanied by the limitations of low skin permeability, while the latter is subject to the liver first-pass effect and may induce systemic side effects. Recently, microneedle technique has provided a new paradigm for efficient transdermal drug delivery, which can break through the skin stratum corneum to create multiple micron-level channels, significantly improving the transdermal drug penetration. Controlling the length of microneedles helps to avoid touching the rich capillaries and nerve endings in the dermis, eliminating the pain associated with the administration.

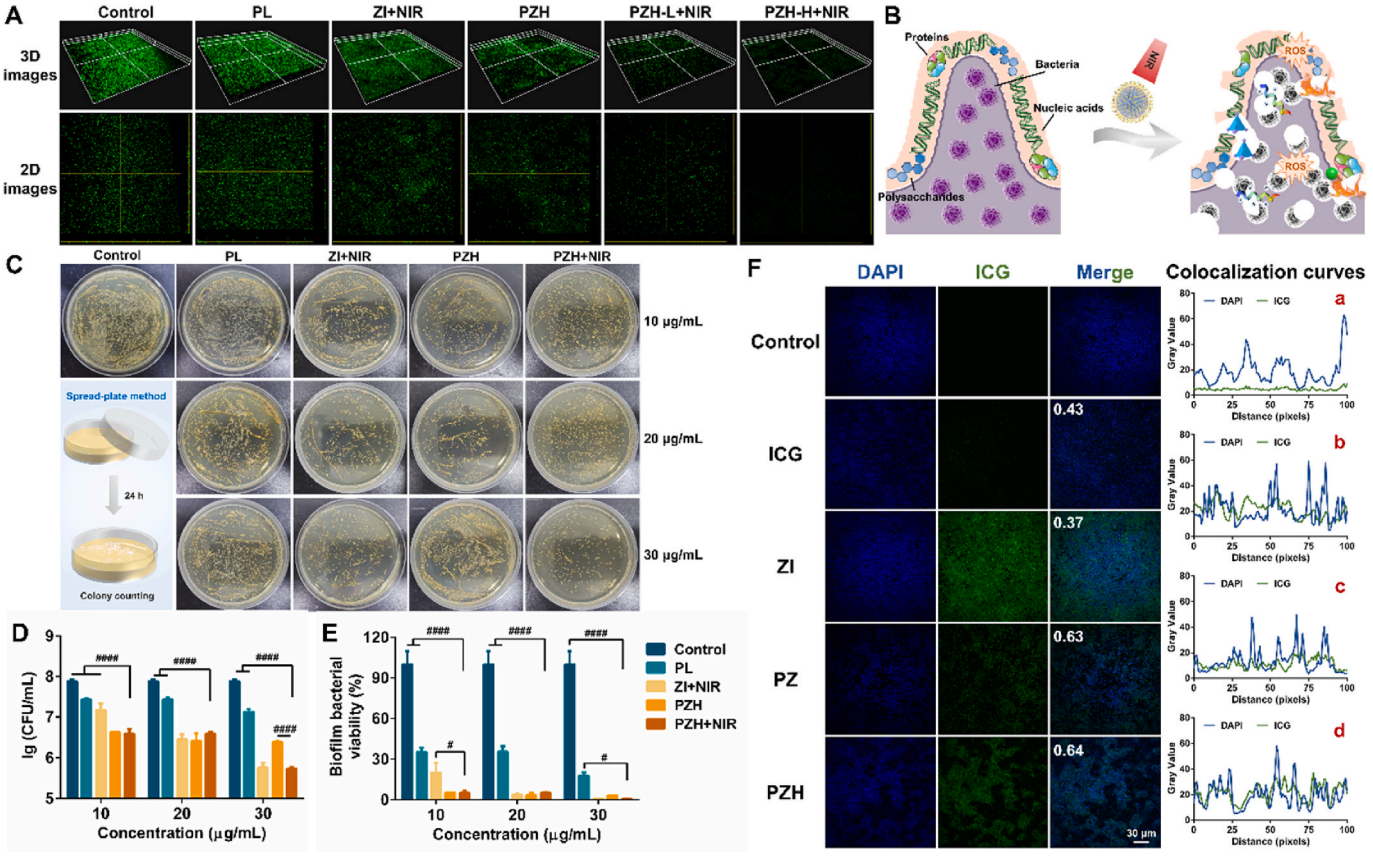

Fig. 3. *In vitro* anti-biofilm and penetration performances. (A) 3D and 2D images of SYTO 9-stained MRSA biofilm after various treatments. (B) Schematic diagram of anti-biofilm mechanisms of PZH nanosystem. (C) Images of residue MRSA in biofilm spread on agar plates. (D) The number of viable MRSA bacteria in biofilm after treatments ($n = 3$). Note: $^{\#\#\#\#}p < 0.0001$ *vs* PZH + NIR. (E) The biofilm bacterial viability relative to the control group ($n = 3$). Note: $^{\#}p < 0.05$ *vs* PZH + NIR, $^{\#\#\#\#}p < 0.0001$ *vs* PZH + NIR. (F) The penetration of free drug or different nanoparticles into MRSA biofilm (scale bar: 30 μm), and the corresponding colocalization curve in each group: a) free ICG, b) ZI, c) PZ, d) PZH.

Based on the above considerations, PZH nanoparticles were packed into MNs for transdermal delivery to the topical bacterial skin infection. When MNs were applied to the skin, the MNs matrix would be dissolved by the interstitial fluid, so the encapsulated NPs were released to the target lesion site to perform their functions. The microneedles patch was composed of 144 single needles (12 × 12 array) on a backing layer. A multi-step centrifugation method was employed to fabricate PZH MNs, as illustrated in Fig. 4A. The SEM image of PZH MNs in Fig. 4B depicted the microscopic morphology of one needle with 1200 μm in height and 300 μm in width, without any cracks or defects. Blank MNs in Fig. S19 displayed smooth needle tips, whereas it could be clearly observed that the nanoparticles were almost deposited on the needle tips in PZH MNs (Fig. 4C and D) and PZ MNs (Fig. S20). Furthermore, the digital photograph (Fig. 4E) showed the green NPs homogeneously distributed in the needle tips of MNs, which was conducive to the deeper penetration of the PZH nanosystem to lesion sites after skin puncture. The micrograph in Fig. 4F and the 3D reconstruction fluorescence image in Fig. 4G of PZH MNs also revealed the same conclusion.

Microneedles should possess good mechanical strength for insertion into the skin while resisting fracture. As reported, the force required for each needle to penetrate the skin stratum corneum was less than 0.1 N [51]. As shown in Fig. 4H and I, the fracture forces of the four types of NPs-embedded MNs patches were similar with all more than 250 N, significantly greater than the minimum force required to puncture the skin. Then, one piece of PZH MNs was pressed to the mouse back skin, and the created orderly arranged array of micropores could be distinctly observed in Fig. 4J with a penetration rate above 95 %. Microchannels also could be found in the H&E-stained skin tissue after microneedle puncture for ZI MNs (Fig. S21) and PZH MNs (Fig. 4K). Additionally, it was found that the needles on the backing layer thoroughly dissolved

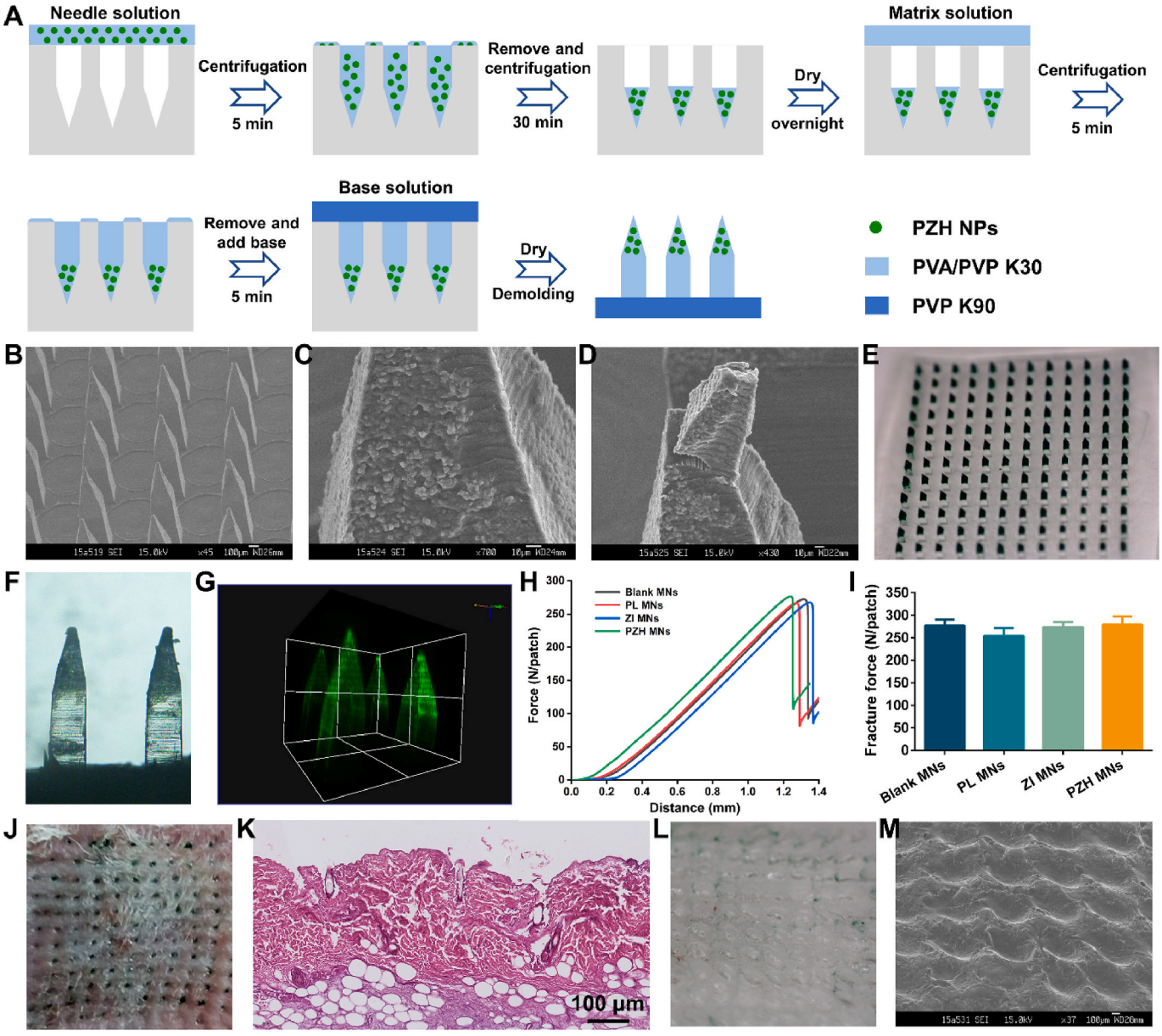

Fig. 4. Fabrication and characterization of PZH MNs. (A) Schematic illustration of the preparation procedures for PZH MNs. (B–D) SEM images of PZH MNs (scale bar: 100 μm and 10 μm). (E) Digital photograph of PZH MNs patch. (F) The micrograph of PZH MNs under bright field. (G) The 3D reconstruction fluorescence image of PZH MNs. (H) A function of the force and distance recorded by a texture analyzer. (I) The fracture forces of various MNs ($n = 3$). (J) The photograph of mouse back skin after insertion of PZH MNs. (K) Corresponding H&E staining section of inserted rat skin (scale bar: 100 μm). (L) The digital photograph and (M) SEM image of PZH MNs after rat skin insertion for 2 min.

after skin insertion (Fig. 4L and M). Collectively, the obtained PZH MNs possessed enough mechanical strength to pierce the skin and rapid dissolution capacity to release the payload.

3.9. The photothermal performance and stability of PZH MNs

The photothermal conversion ability of the prepared MNs was assessed. For the blank MNs, there was no significant temperature change under the 808 nm NIR irradiation with an output density of 1.0 W/cm^2 (Fig. 5A and B). In contrast, the temperature of PZH MNs soared to ~96 °C after exposure to the same NIR laser for only 1 min, and it was maintained stable at around 100 °C for the next 20 min. As depicted in Fig. 5C and D, the temperature was enhanced to 39 °C, 58 °C, 80 °C, and 108 °C with the increasing laser power densities from 0.3 to 1.0 W/cm^2, respectively. These results demonstrated the feasibility of controlling the heating effect for PZH MNs, and that the outstanding photothermal conversion ability of PZH NPs would not be altered after integration into the MNs.

Next, we further corroborated whether encapsulation in MNs would affect the structure of the PZH NPs. The hydrodynamic size of PZH was determined to increase slightly to 174.7 nm after being loaded into microneedles (no statistical difference), revealing the presence of intact nanostructure (Fig. 5E). As shown in Fig. 5F and G, the drug loading of ICG and PL in PZH MNs remained essentially stable after storage at room temperature, with no statistical difference relative to day 0. This should be attributed to that the nanoparticle structure helped to maintain the ultrahigh stability of the ICG and PL payloads in microneedles.

3.10. In vivo anti-MRSA infection studies

Drug-resistant MRSA often causes recurrent and persistent skin infections that are hard to cure and eradicate. Thereby in this study, an animal model of back skin abscess was established. As shown in Fig. S22, 24 h after subcutaneous inoculation of MRSA bacteria, a prominent red and swollen protrusion was observed on both the front and side. The lesion site was then excised and the area was found to be severely infected with a yellowish abscess, indicating successful modeling.

For the photothermal groups, the temperature increased under NIR light irradiation after MNs administration (Fig. 6A and B). After administration of PZH MNs plus laser irradiation, the average skin abscess surface temperature of mice was around 48–52 °C, indicating that PZH MNs could induce moderate hyperthermia and avoid affecting the surrounding normal tissues. The groups of ZI MNs + NIR and PZ MNs + NIR also resulted in a similar heating effect. As a topical antibiotic for skin infections, mupirocin ointment acted as a positive control. At the end of the treatment, the infected site skin was collected as presented in Fig. 6C that the control group showed the most severe subcutaneous infection and necrosis, whereas the infection was largely relieved and closest to the normal skin in the PZH MNs + NIR group. Other groups also showed some degree of remission. Then the excised lesion sites were

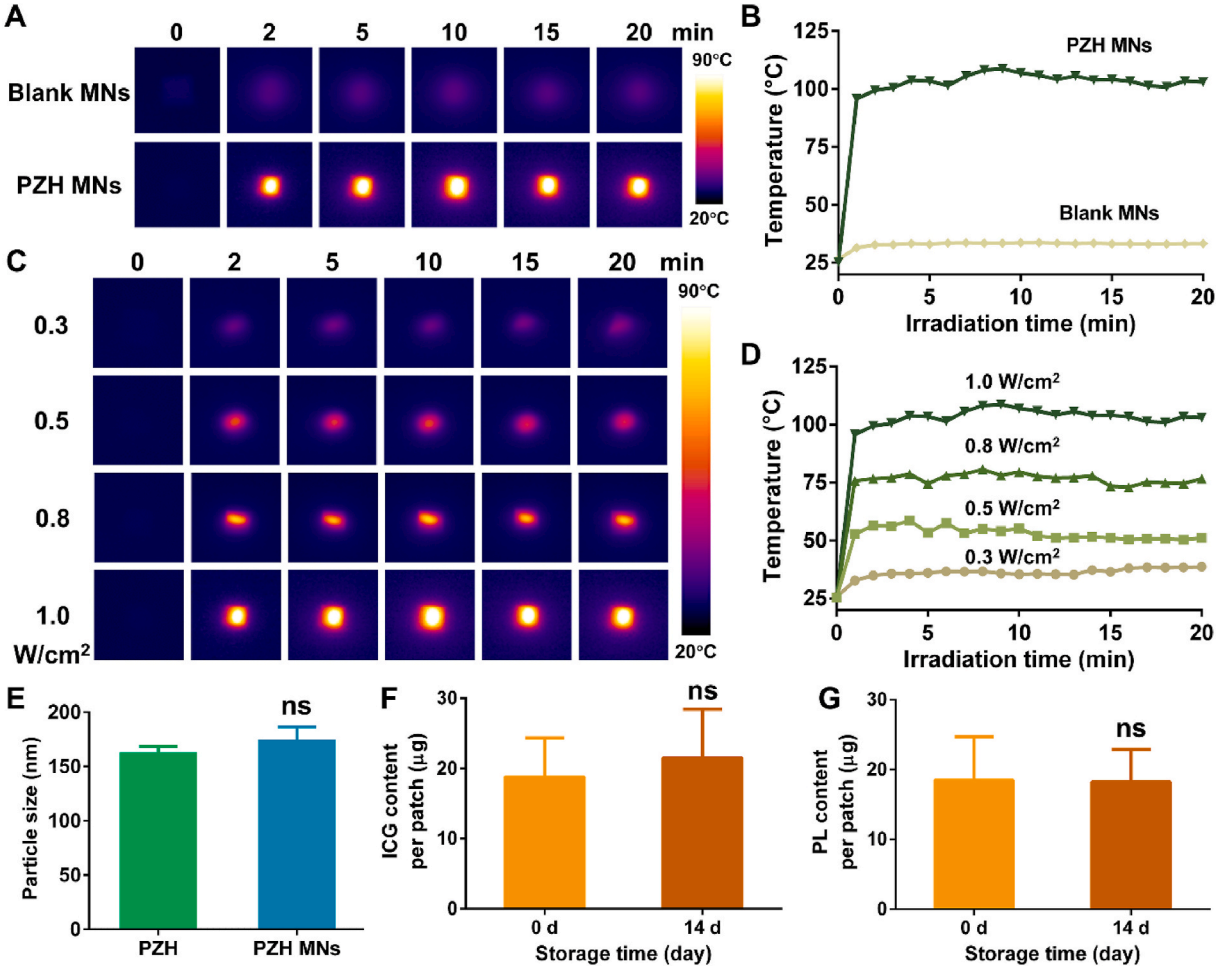

Fig. 5. The photothermal performance and stability of PZH MNs. (A) The thermographic images and (B) temperature change curves of blank MNs and PZH MNs under 808 nm NIR laser irradiation at 1.0 W/cm^2 (C)The thermographic images and (D) temperature change curves of PZH MNs under 808 nm laser irradiation at different power intensities. (E) The hydrodynamic size of PZH before and after loaded in microneedles ($n = 3$). The amount of (F) ICG and (G) PL in PZH MNs after storage for 14 d ($n = 3$). Note: ns signified no significant difference.

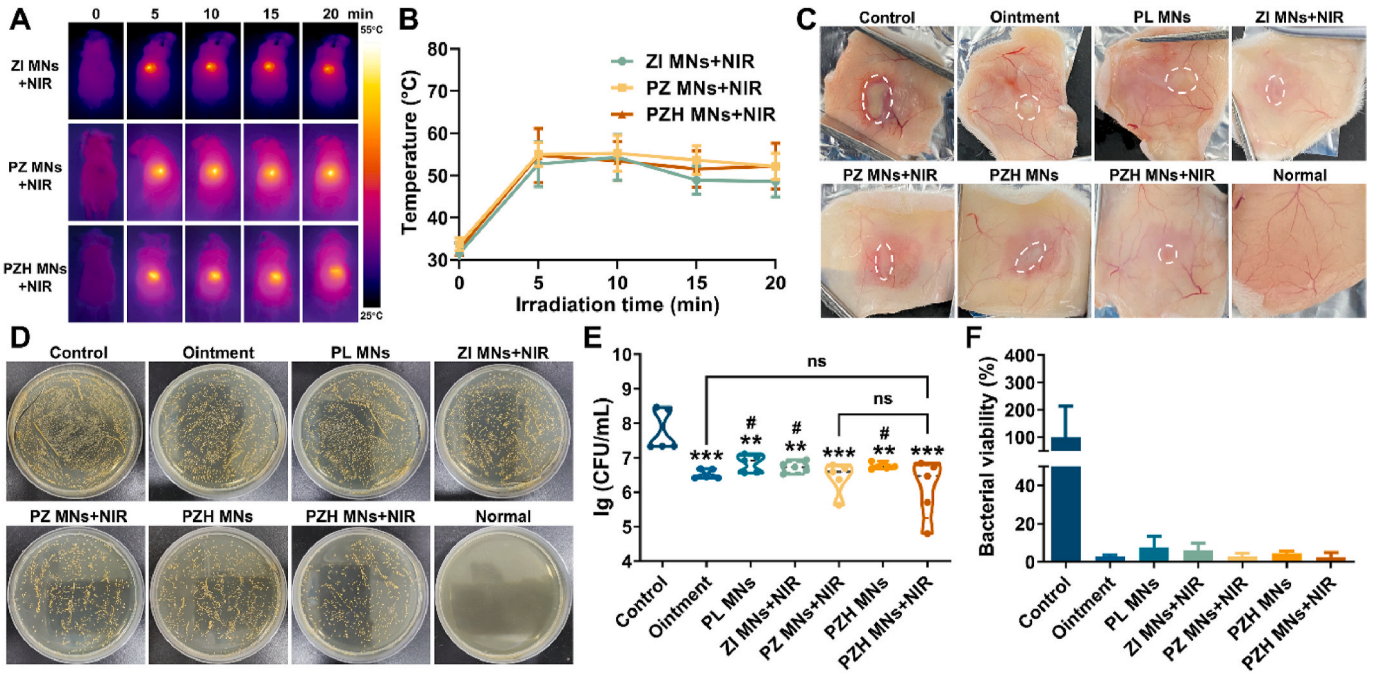

Fig. 6. *In vivo* photothermal conversion and anti-MRSA performances. (A) Near-infrared photothermal images of mice. (B) The local temperature curves of the infected skin ($n = 5$). (C) Representative images showing the subcutaneous abscess in MRSA-infected skin after different treatments. (D) Photographic images of *in vivo* MRSA colonies cultured on agar plates. (E) The number of *in vivo* viable MRSA that expressed as lg (CFU/mL) ($n = 5$). Note: ns signified no significant difference *vs* control, $^{**}p < 0.01$ *vs* control, $^{***}p < 0.001$ *vs* control, $^{\#}p < 0.05$ *vs* PZH MNs + NIR. (F) The bacterial survival rate relative to the control ($n = 5$).

homogenized and cultured on agar plates to visualize the density of alive MRSA bacteria. As shown in Fig. 6D, no target MRSA colonies were present on the normal skin. The untreated control group had a high number of viable bacteria in dense growth. In contrast, after treatment with mupirocin ointment or different MNs, the growth of MRSA colonies was significantly less than that in the control group. In particular, the bacterial growth condition of PZH MNs + NIR was more inhibited, with the relatively least number of viable bacteria surviving. Then the viable bacterial colony number was quantified. As shown in Fig. 6E and F, the untreated control group presented the highest logarithmic value of viable bacteria at approximately 7.77 lg, and the mupirocin ointment group displayed a decrease of 1.24 lg ($^{***}p < 0.001$) compared to the control. For the groups exerting monotherapy, a decrease of 0.93 lg, 1.04 lg, and 1.02 lg ($^{**}p < 0.01$ for all) was achieved for PL MNs, ZI MNs + NIR, and PZH MNs, respectively. As expected, the PZH MNs + NIR group significantly minimized the number of residual MRSA with 1.67 lg colonial reduction ($^{***}p < 0.001$ vs control) and presented the highest germicidal effect (~97.50 %) among all the seven groups. It demonstrated the effective inhibition of MRSA growth by the triple therapy of PZH MNs plus NIR irradiation.

3.11. *In vivo inflammatory response and histological analysis*

For bacterial infections, pyrogens including the bacteria themselves and their metabolites will induce the inflammatory response. Thus, the expression levels of pro-inflammatory cytokines (mainly IL-6 and TNF-α) were determined to assess the anti-inflammatory effect (Fig. 7A–C). For IL-6, the average concentration was decreased from 940 pg/mL in the control group to 258 and 233 pg/mL in commercial ointment and PZH MNs + NIR, respectively. In like manner, the expression of TNF-α was the least after being treated by PZH MNs + NIR, while there was no significant difference between the ointment and control group.

Histological analysis of the infected skin was performed, and the H&E staining results were shown in Fig. 7D. In the control group, acute and chronic inflammatory cells, mainly neutrophils, had infiltrated into the dermis. The presence of distinct inflammatory foci and massive necrotic areas indicated the typical inflammatory response. In contrast, fewer neutrophil aggregates were observed in the treatment groups, among which PZH MNs + NIR displayed the least inflammatory infiltration. The histological morphology of skin sections treated with the PZH MNs + NIR group was closest to that of the normal healthy group, with arranged epidermal cells and no collagen fiber breakage. As one of the Gram-positive bacteria, MRSA could be stained blue-purple by Gram staining. In Fig. 7E, a large amount of blue-purple dye was deposited in the skin section of the control group, indicating the presence of alive MRSA bacteria. Regarding the treated skin by PZH MNs plus NIR, a conspicuous alleviation of bacterial infection could be observed in comparison with other groups, implying the potent inhibition of MRSA growth by the triple therapy. The H&E staining of main organs (including heart, liver, spleen, lung, and kidney) showed that no substantial organ lesions or damage were observed in all groups, without appreciable inflammatory cells (Fig. S23).

Combining the above results, the application of MNs would not affect the normal tissues and meanwhile contributed to the transdermal delivery of the PZH nanosystem. PZH MNs plus NIR could not only eradicate bacterial proliferation but also alleviate the inflammatory response, which functioned by working along both lines against MRSA-induced skin infection.

3.12. *In vivo safety evaluation*

Inspired by the superior antimicrobial efficacy of PZH MNs, the *in vivo* biocompatibility was further investigated to illustrate the potential for clinical treatment. First, the short-term and long-term toxicity of PZH MNs and PZH aq were assessed *in vivo*. As shown in Fig. 8A, the skin sections in both groups showed no abnormal morphological changes after 5 h or 5 d of administration, which was typified by well-defined epidermal and dermal structures. Then the cumulative toxicity was figured out by collecting major organs for morphological analysis (Fig. 8B). Not any pathological changes (inflammation, fibrosis, etc.) were observed after short-term and long-term administration in comparison with healthy tissue.

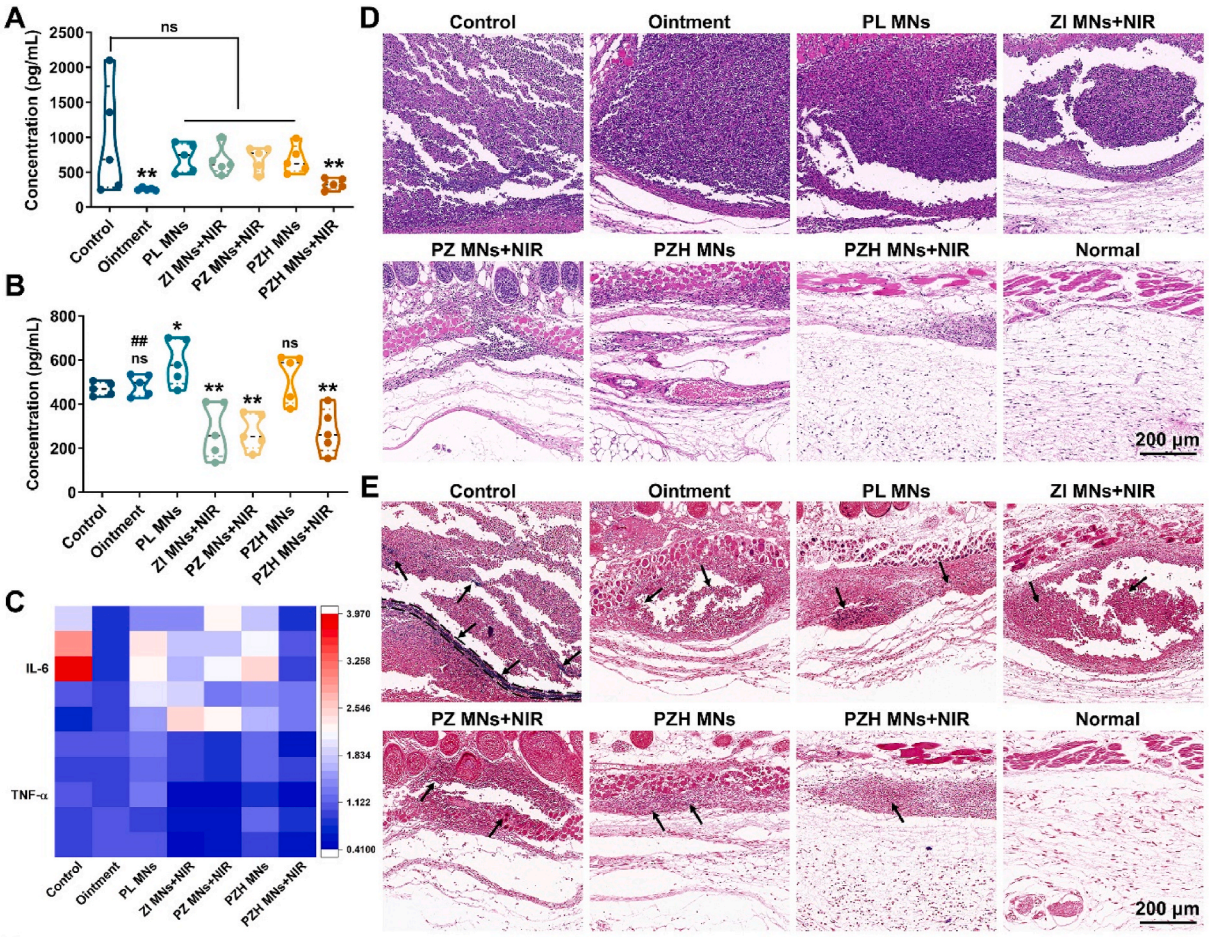

Fig. 7. *In vivo* inflammatory response and histological analysis. The expression level of (A) IL-6 and (B) TNF-α determined via ELISA kit ($n = 5$). Note: ns signified no significant difference *vs* control, $^{*}p < 0.05$ *vs* control, $^{**}p < 0.01$ *vs* control, $^{\#\#}p < 0.01$ *vs* PZH MNs + NIR. (C) The heatmap of pro-inflammatory cytokine expression ($n = 5$). (D) H&E and (E) Gram-stained sections of infected skin tissues. The black arrows indicated the presence of Gram-positive bacteria (stained blue-purple, scale bar: 200 μm).

Blood routine tests were performed to explore their hemocompatibility. After 5 h of administration, the level of neutrophils slightly elevated, while lymphocytes and eosinophils showed decreased levels in PZH MNs, but it was generally manageable (Fig. S24). Five days after dosing, the levels of white blood cells, red blood cells, hemoglobin, platelets, lymphocytes, neutrophils, and monocytes in the groups of PZH MNs and PZH aq were not significantly different compared to healthy mice (Fig. S25), implying the application of PZH and MNs did not produce hemolytic anemia, inflammation, coagulation dysfunction, or other side effects.

Finally, Fig. S26 displayed the skin recovery on the back of mice after treatment with blank MNs and PZH MNs. Both groups of mice showed distinct puncture pores and slight redness on the skin surface just after MNs insertion. Then, the skin gradually returned to normal about 1 d later, indicating that the MN patches could be tolerated with sound safety.

4. Conclusion

This study provided a facile and effective triple therapy strategy against multidrug-resistant bacteria and biofilms by constructing versatile MOFs-based "on-demand" nanosystem-integrated microneedles. The fabricated PZH MNs could pierce the skin stratum corneum for enhanced transdermal drug delivery into topical bacterial skin infection and physical puncture of the bacterial biofilms. After the nanoparticles were released from MNs, the outer HA layer in response to bacterial infection micromilieu endowed the nanosystem with selective targeting and enhanced biosafety. Under pH/NIR dual stimuli, PL first disrupted the bacterial membrane integrity, ICG-induced local hyperthermia and cytotoxic ROS resulted in the dysfunction of intracellular components, and zinc ions disturbed ion balance and generated free radicals. Meanwhile, the bacterial metabolism was intercepted by blocking the ATP synthesis process. *In vitro* and *in vivo* experiments validated the amplified antimicrobial and anti-inflammatory effect of the PZH nanoplatform, which also displayed a superior biofilm destruction ability (>99.30 % eradication). Looking forward, the three-in-one nanosystem-integrated MNs fosters a novel antibiotics-free avenue for combating bacterial infection and biofilm growth, promising for future biomedical applications.

CRediT authorship contribution statement

Ting Wen: Writing – original draft, Visualization, Validation, Software, Methodology, Investigation, Formal analysis, Data curation, Conceptualization. **Yiting Zhao:** Visualization, Software, Methodology, Investigation, Formal analysis, Data curation. **Yanping Fu:** Visualization, Validation, Resources, Investigation, Formal analysis, Data curation. **Ying Chen:** Methodology, Formal analysis, Data curation. **Xiaodie Li:** Resources, Methodology, Data curation. **Chaonan Shi:** Validation, Investigation, Formal analysis. **Dongyi Xian:** Visualization, Data curation. **Wanchen Zhao:** Validation. **Dan Yang:** Data curation. **Chao Lu:** Software. **Chuanbin Wu:** Software. **Xin Pan:** Writing – review &

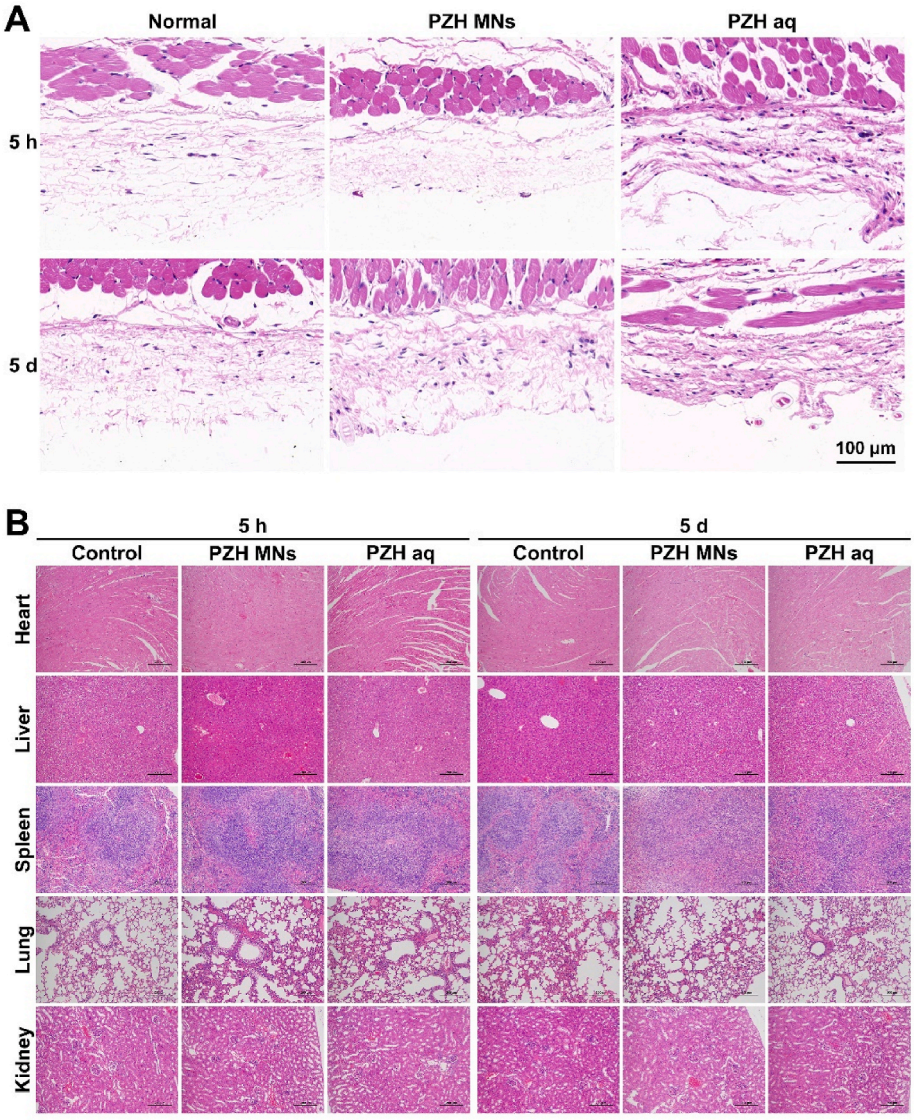

Fig. 8. H&E staining of (A) topical skin tissues and (B) major organs after short-term and long-term treatments (scale bar: 100 & 200 μm).

editing, Supervision, Project administration, Methodology. **Guilan Quan:** Writing – review & editing, Supervision, Resources, Project administration, Funding acquisition.

Declaration of competing interest

The authors declare the following financial interests/personal relationships which may be considered as potential competing interests: Quan, Guilan reports financial support provided by the National Natural Science Foundation of China. Quan, Guilan reports financial support provided by the Special Fund Project for Science and Technology Innovation Strategy of Guangdong Province. Quan, Guilan reports financial support provided by the Guangzhou Science and Technology Plan Project. If there are other authors, they declare that they have no known competing financial interests or personal relationships that could have appeared to influence the work reported in this paper.

Acknowledgments

This work was supported by the National Natural Science Foundation of China [Grant No. 82173747], the Special Fund Project for Science and Technology Innovation Strategy of Guangdong Province [Grant No. 2021TQ060944], and the Guangzhou Science and Technology Plan Project [Grant No. 2024A04J9956].

Appendix A. Supplementary data

Supplementary data to this article can be found online at https://doi.org/10.1016/j.mtbio.2024.101327.

Data availability

Data will be made available on request.

References

[1] Y. Liu, Y. Jia, K. Yang, R. Li, X. Xiao, K. Zhu, Z. Wang, Metformin restores tetracyclines susceptibility against multidrug resistant bacteria, Adv. Sci. 7 (12) (2020) 1902227, https://doi.org/10.1002/advs.201902227.

[2] Z. Yuan, C. Lin, L. Dai, Y. He, J. Hu, K. Xu, B. Tao, P. Liu, K. Cai, Near-infrared light-activatable dual-action nanoparticle combats the established biofilms of methicillin-resistant *Staphylococcus aureus* and its accompanying inflammation, Small 17 (13) (2021) e2007522, https://doi.org/10.1002/smll.202007522.

[3] R.A. Mustafa, P. Parkkila, J.M. Rosenholm, H.B. Zhang, T. Viitala, Monitoring silica core@shell nanoparticle-bacterial film interactions using the multi-parametric surface plasmon resonance technique, Smart Med. 2 (3) (2023) 16, https://doi.org/10.1002/smmd.20230012.

[4] F. Pan, G. Giovannini, S.X. Zhang, S. Altenried, F. Zuber, Q. Chen, L.F. Boesel, Q. Ren, pH-responsive silica nanoparticles for the treatment of skin wound infections, Acta Biomater. 145 (2022) 172–184, https://doi.org/10.1016/j.actbio.2022.04.009.
[5] M.T. Ou, C.C. Lin, Y. Wang, Y.T. Lu, W.Y. Wang, Z.M. Li, W.W. Zeng, X.W. Zeng, X. Y. Ji, L. Mei, Heterojunction engineered bioactive chlorella for cascade promoted cancer therapy, J. Contr. Release 345 (2022) 755–769, https://doi.org/10.1016/j.jconrel.2022.03.059.
[6] W. Zhang, X. Hu, Q. Shen, D. Xing, Mitochondria-specific drug release and reactive oxygen species burst induced by polyprodrug nanoreactors can enhance chemotherapy, Nat. Commun. 10 (1) (2019) 1704, https://doi.org/10.1038/s41467-019-09566-3.
[7] Q. Gao, D. Huang, Y. Deng, W. Yu, Q. Jin, J. Ji, G. Fu, Chlorin e6 (Ce6)-loaded supramolecular polypeptide micelles with enhanced photodynamic therapy effect against *Pseudomonas aeruginosa*, Chem. Eng. J. 417 (2021) 129334, https://doi.org/10.1016/j.cej.2021.129334.
[8] T. Xie, Y. Qi, Y. Li, F. Zhang, W. Li, D. Zhong, Z. Tang, M. Zhou, Ultrasmall Ga-ICG nanoparticles based gallium ion/photodynamic synergistic therapy to eradicate biofilms and against drug-resistant bacterial liver abscess, Bioact. Mater. 6 (11) (2021) 3812–3823, https://doi.org/10.1016/j.bioactmat.2021.03.032.
[9] Y. Zhou, B. Niu, Y. Zhao, J. Fu, T. Wen, K. Liao, G. Quan, X. Pan, C. Wu, Multifunctional nanoreactors-integrated microneedles for cascade reaction-enhanced cancer therapy, J. Contr. Release 339 (2021) 335–349, https://doi.org/10.1016/j.jconrel.2021.09.041.
[10] H. Qiu, S. Zhu, L. Pang, J. Ma, Y. Liu, L. Du, Y. Wu, Y. Jin, ICG-loaded photodynamic chitosan/polyvinyl alcohol composite nanofibers: anti-resistant bacterial effect and improved healing of infected wounds, Int. J. Pharm. 588 (2020) 119797, https://doi.org/10.1016/j.ijpharm.2020.119797.
[11] Z. Chaudhary, G.M. Khan, M.M. Abeer, N. Pujara, B. Wan-Chi Tse, M.A. McGuckin, A. Popat, T. Kumeria, Efficient photoacoustic imaging using indocyanine green (ICG) loaded functionalized mesoporous silica nanoparticles, Biomater. Sci. 7 (12) (2019) 5002–5015, https://doi.org/10.1039/c9bm00822e.
[12] X. Zhang, Y. Li, M. Wei, C. Liu, T. Yu, J. Yang, Cetuximab-modified silica nanoparticle loaded with ICG for tumor-targeted combinational therapy of breast cancer, Drug Deliv. 26 (1) (2019) 129–136, https://doi.org/10.1080/10717544.2018.1564403.
[13] Q. Chen, L. Xu, C. Liang, C. Wang, R. Peng, Z. Liu, Photothermal therapy with immune-adjuvant nanoparticles together with checkpoint blockade for effective cancer immunotherapy, Nat. Commun. 7 (2016) 13193, https://doi.org/10.1038/ncomms13193.
[14] R. Li, T. Chen, X. Pan, Metal-organic-framework-based materials for antimicrobial applications, ACS Nano 15 (3) (2021) 3808–3848, https://doi.org/10.1021/acsnano.0c09617.
[15] X.W. Geng, N. Zhang, Z.R. Li, M.Y. Zhao, H.B. Zhang, J.G. Li, Iron-doped nanozymes with spontaneous peroxidase-mimic activity as a promising antibacterial therapy for bacterial keratitis, Smart Med 3 (2) (2024) 13, https://doi.org/10.1002/smmd.20240004.
[16] J.Y. Shan, J.Y. Che, C.H. Song, Y.J. Zhao, Emerging antibacterial nanozymes for wound healing, Smart Med. 2 (3) (2023) 14, https://doi.org/10.1002/smmd.20220025.
[17] T. Wen, G. Quan, B. Niu, Y. Zhou, Y. Zhao, C. Lu, X. Pan, C. Wu, Versatile nanoscale metal-organic frameworks (nMOFs): an emerging 3D nanoplatform for drug delivery and therapeutic applications, Small 17 (8) (2021) e2005064, https://doi.org/10.1002/smll.202005064.
[18] B. Wu, J. Fu, Y. Zhou, J. Wang, X. Feng, Y. Zhao, G. Zhou, C. Lu, G. Quan, X. Pan, C. Wu, Metal-organic framework-based chemo-photothermal combinational system for precise, rapid, and efficient antibacterial therapeutics, Pharmaceutics 11 (9) (2019) 463, https://doi.org/10.3390/pharmaceutics11090463.
[19] T. Wen, Z. Lin, Y. Zhao, Y. Zhou, B. Niu, C. Shi, C. Lu, X. Wen, M. Zhang, G. Quan, C. Wu, X. Pan, Bioresponsive nanoarchitectonics-integrated microneedles for amplified chemo-photodynamic therapy against acne vulgaris, ACS Appl. Mater. Interfaces 13 (41) (2021) 48433–48448, https://doi.org/10.1021/acsami.1c15673.
[20] Z. Wang, X. Liu, Y. Duan, Y. Huang, Infection microenvironment-related antibacterial nanotherapeutic strategies, Biomaterials 280 (2022) 121249, https://doi.org/10.1016/j.biomaterials.2021.121249.
[21] D. Han, X. Liu, S. Wu, Metal organic framework-based antibacterial agents and their underlying mechanisms, Chem. Soc. Rev. 51 (16) (2022) 7138–7169, https://doi.org/10.1039/d2cs00460g.
[22] Y. Huang, H. Geng, Z. Wu, L. Sun, C. Ji, C.A. Grimes, X. Feng, Q. Cai, An Ag_2S@ZIF-Van nanosystem for NIR-II imaging of bacterial-induced inflammation and treatment of wound bacterial infection, Biomater. Sci. 10 (14) (2022) 3972–3980, https://doi.org/10.1039/d2bm00550f.
[23] X. Zhang, L. Liu, L. Huang, W. Zhang, R. Wang, T. Yue, J. Sun, G. Li, J. Wang, The highly efficient elimination of intracellular bacteria via a metal organic framework (MOF)-based three-in-one delivery system, Nanoscale 11 (19) (2019) 9468–9477, https://doi.org/10.1039/c9nr01284b.
[24] Y. Zheng, Y. Yan, L. Lin, Q. He, H. Hu, R. Luo, D. Xian, J. Wu, Y. Shi, F. Zeng, C. Wu, G. Quan, C. Lu, Titanium carbide MXene-based hybrid hydrogel for chemo-photothermal combinational treatment of localized bacterial infection, Acta Biomater. 142 (2022) 113–123, https://doi.org/10.1016/j.actbio.2022.02.019.
[25] L. Zhou, H. Zheng, Z. Liu, S. Wang, Z. Liu, F. Chen, H. Zhang, J. Kong, F. Zhou, Q. Zhang, Conductive antibacterial hemostatic multifunctional scaffolds based on $Ti_3C_2T_x$ MXene nanosheets for promoting multidrug-resistant bacteria-infected wound healing, ACS Nano 15 (2) (2021) 2468–2480, https://doi.org/10.1021/acsnano.0c06287.
[26] X.Q. Feng, D.Y. Xian, J.T. Fu, R. Luo, W.H. Wang, Y.W. Zheng, Q. He, Z. Ouyang, S. B. Fang, W.C. Zhang, D.J. Liu, S.J. Tang, G.L. Quan, J.F. Cai, C.B. Wu, C. Lu, X. Pan, Four-armed host-defense peptidomimetics-augmented vanadium carbide MXene-based microneedle array for efficient photo-excited bacteria-killing, Chem. Eng. J. 456 (2023) 13, https://doi.org/10.1016/j.cej.2022.141121.
[27] Y. Huang, Q. Gao, X. Li, Y. Gao, H. Han, Q. Jin, K. Yao, J. Ji, Ofloxacin loaded MoS_2 nanoflakes for synergistic mild-temperature photothermal/antibiotic therapy with reduced drug resistance of bacteria, Nano Res. 13 (9) (2020) 2340–2350, https://doi.org/10.1007/s12274-020-2853-2.
[28] B. Van Nieuwenhuyse, D. Van der Linden, O. Chatzis, C. Lood, J. Wagemans, R. Lavigne, K. Schroven, J. Paeshuyse, C. de Magnee, E. Sokal, X. Stephenne, I. Scheers, H. Rodriguez-Villalobos, S. Djebara, M. Merabishvili, P. Soentjens, J.-P. Pirnay, Bacteriophage-antibiotic combination therapy against extensively drug-resistant *Pseudomonas aeruginosa* infection to allow liver transplantation in a toddler, Nat. Commun. 13 (1) (2022) 5725, https://doi.org/10.1038/s41467-022-33294-w.
[29] R.Y.K. Chang, S.C. Nang, H.K. Chan, J. Li, Novel antimicrobial agents for combating antibiotic-resistant bacteria, Adv. Drug Deliv. Rev. 187 (2022) 114378, https://doi.org/10.1016/j.addr.2022.114378.
[30] C. Li, R. Nyaruaba, X. Zhao, H. Xue, Y. Li, H. Yang, H. Wei, Thermosensitive hydrogel wound dressing loaded with bacteriophage lysin LysP53, Viruses 14 (9) (2022) 1956, https://doi.org/10.3390/v14091956.
[31] D. Morais, L. Tanoeiro, A.T. Marques, T. Goncalves, A. Duarte, A.P.A. Matos, J. S. Vital, M.E.M. Cruz, M.C. Carvalheiro, E. Anes, J.M.B. Vitor, M.M. Gaspar, F. F. Vale, Liposomal delivery of newly identified prophage lysins in a *Pseudomonas aeruginosa* model, Int. J. Mol. Sci. 23 (17) (2022) 10143, https://doi.org/10.3390/ijms231710143.
[32] L.S. Biswaro, M.G. da Costa Sousa, T.M.B. Rezende, S.C. Dias, O.L. Franco, Antimicrobial peptides and nanotechnology, recent advances and challenges, Front. Microbiol. 9 (2018) 855, https://doi.org/10.3389/fmicb.2018.00855.
[33] C. Lu, T. Wen, M. Zheng, D. Liu, G. Quan, X. Pan, C. Wu, Poly(Ethylene glycol) crosslinked multi-armed poly(l-lysine) with encapsulating capacity and antimicrobial activity for the potential treatment of infection-involved multifactorial diseases, Pharmaceutics 12 (1) (2020) 14, https://doi.org/10.3390/pharmaceutics12010047.
[34] Y. Liu, D. Huo, X. Zhu, X. Chen, A. Lin, Z. Jia, J. Liu, A ruthenium nanoframe/enzyme composite system as a self-activating cascade agent for the treatment of bacterial infections, Nanoscale 13 (35) (2021) 14900–14914, https://doi.org/10.1039/d1nr02439f.
[35] X. Wei, J. Li, Y. Zhang, Y. Zheng, Y. Zhang, H. Meng, G. Wu, Y. Hu, Y. Gao, S. Huang, W. Wang, Y. Cheng, Z. Wu, X. Zhang, Synergy between clinical microenvironment targeted nanoplatform and near-infrared light irradiation for managing *Pseudomonas aeruginosa* infections, ACS Appl. Mater. Interfaces 13 (33) (2021) 38979–38989, https://doi.org/10.1021/acsami.1c08132.
[36] Y. Gao, J. Wang, M. Chai, X. Li, Y. Deng, Q. Jin, J. Ji, Size and charge adaptive clustered nanoparticles targeting the biofilm microenvironment for chronic lung infection management, ACS Nano 14 (5) (2020) 5686–5699, https://doi.org/10.1021/acsnano.0c00269.
[37] R. Jamaledin, C.K.Y. Yiu, E.N. Zare, L.N. Niu, R. Vecchione, G. Chen, Z. Gu, F. R. Tay, P. Makvandi, Advances in antimicrobial microneedle patches for combating infections, Adv. Mater. 32 (33) (2020) e2002129, https://doi.org/10.1002/adma.202002129.
[38] J. Xu, R. Danehy, H. Cai, Z. Ao, M. Pu, A. Nusawardhana, D. Rowe-Magnus, F. Guo, Microneedle patch-mediated treatment of bacterial biofilms, ACS Appl. Mater. Interfaces 11 (16) (2019) 14640–14646, https://doi.org/10.1021/acsami.9b02578.
[39] S.B. Li, X.M. Wang, Z.Y. Yan, T. Wang, Z.B. Chen, H. Song, Y.B. Zheng, Microneedle patches with antimicrobial and immunomodulating properties for infected wound healing, Adv. Sci. 10 (22) (2023) 12, https://doi.org/10.1002/advs.202300576.
[40] Y. Zhang, P. Sun, L. Zhang, Z. Wang, F. Wang, K. Dong, Z. Liu, J. Ren, X. Qu, Silver-infused porphyrinic metal-organic framework: surface-adaptive, on-demand nanoplatform for synergistic bacteria killing and wound disinfection, Adv. Funct. Mater. 29 (11) (2019) 1808594, https://doi.org/10.1002/adfm.201808594.
[41] J. Liu, R.S. Li, M. He, Z. Xu, L.Q. Xu, Y. Kang, P. Xue, Multifunctional SGQDs-CORM@HA nanosheets for bacterial eradication through cascade-activated "nanoknife" effect and photodynamic/CO gas therapy, Biomaterials 277 (2021) 121084, https://doi.org/10.1016/j.biomaterials.2021.121084.
[42] F. Zhang, J. Zhuang, Z. Li, H. Gong, B.E. de Ávila, Y. Duan, Q. Zhang, J. Zhou, L. Yin, E. Karshalev, W. Gao, V. Nizet, R.H. Fang, L. Zhang, J. Wang, Nanoparticle-modified microrobots for in vivo antibiotic delivery to treat acute bacterial pneumonia, Nat. Mater. 21 (11) (2022) 1324, https://doi.org/10.1038/s41563-022-01360-9.
[43] Y. Zhao, Y. Zhou, D. Yang, X. Gao, T. Wen, J. Fu, X. Wen, G. Quan, X. Pan, C. Wu, Intelligent and spatiotemporal drug release based on multifunctional nanoparticle-integrated dissolving microneedle system for synergetic chemo-photothermal therapy to eradicate melanoma, Acta Biomater. 135 (2021) 164–178, https://doi.org/10.1016/j.actbio.2021.09.009.
[44] B. Yang, Y. Dong, Y. Shen, A. Hou, G. Quan, X. Pan, C. Wu, Bilayer dissolving microneedle array containing 5-fluorouracil and triamcinolone with biphasic release profile for hypertrophic scar therapy, Bioact. Mater. 6 (8) (2021) 2400–2411, https://doi.org/10.1016/j.bioactmat.2021.01.014.
[45] A. Hou, G. Quan, B. Yang, C. Lu, M. Chen, D. Yang, L. Wang, H. Liu, X. Pan, C. Wu, Rational design of rapidly separating dissolving microneedles for precise drug delivery by balancing the mechanical performance and disintegration rate, Adv. Healthcare Mater. 8 (21) (2019) e1900898, https://doi.org/10.1002/adhm.201900898.

[46] B. Wang, N. Zhang, W.C. Feng, S. Chen, X.Y. Zhu, X.H. Shan, R.Z. Yuan, B. Yuan, H. Z. Wang, G. Zhou, J. Liu, X.Y. Sun, Gallium nanostructure-based microneedle patch for multidrug-resistant bacterial wound healing: enhanced metal release and NIR photothermal effect, Adv. Funct. Mater. 16 (2024), https://doi.org/10.1002/adfm.202407934.

[47] Y. Li, X. Liu, B. Li, Y. Zheng, Y. Han, D.F. Chen, K.W.K. Yeung, Z. Cui, Y. Liang, Z. Li, S. Zhu, X. Wang, S. Wu, Near-infrared light triggered phototherapy and immunotherapy for elimination of methicillin-resistant *Staphylococcus aureus* biofilm infection on bone implant, ACS Nano 14 (7) (2020) 8157–8170, https://doi.org/10.1021/acsnano.0c01486.

[48] Q. Xu, Y. Hua, Y. Zhang, M. Lv, H. Wang, Y. Pi, J. Xie, C. Wang, Y. Yong, A biofilm microenvironment-activated single-atom iron nanozyme with NIR-controllable nanocatalytic activities for synergetic bacteria-infected wound therapy, Adv. Healthcare Mater. 10 (22) (2021) e2101374, https://doi.org/10.1002/adhm.202101374.

[49] T. Cui, S. Wu, Y. Sun, J. Ren, X. Qu, Self-propelled active photothermal nanoswimmer for deep-layered elimination of biofilm in vivo, Nano Lett. 20 (10) (2020) 7350–7358, https://doi.org/10.1021/acs.nanolett.0c02767.

[50] M. Xu, Y. Hu, Y. Xiao, Y. Zhang, K. Sun, T. Wu, N. Lv, W. Wang, W. Ding, F. Li, B. Qiu, J. Li, Near-infrared-controlled nanoplatform exploiting photothermal promotion of peroxidase-like and OXD-like activities for potent antibacterial and anti-biofilm therapies, ACS Appl. Mater. Interfaces 12 (45) (2020) 50260–50274, https://doi.org/10.1021/acsami.0c14451.

[51] D.D. Zhu, B.Z. Chen, M.C. He, X.D. Guo, Structural optimization of rapidly separating microneedles for efficient drug delivery, J Ind. Eng. Chem. 51 (2017) 178–184, https://doi.org/10.1016/j.jiec.2017.02.030.